Composites Part B 298 (2025) 112354

Contents lists available at ScienceDirect

Composites Part B

journal homepage: www.elsevier.com/locate/composites

From nanoscale to printed products: Multiscale modeling and experimental characterization of graphene-enhanced polylactic acid composites for 3D printing

Atta Muhammad [a,d,1], Clara Valero [b,1], Paolo De Angelis [a,1], Nikolaos Koutroumanis [f], Dionisis Semitekolos [g], Bárbara Jiménez [b], Rubén Rivera [b], Carlos Sáenz Ezquerro [b], Rajat Srivastava [a,e], Panagiotis-Nektarios Pappas [f], Costas Galiotis [f], Costas A. Charitidis [g], Eliodoro Chiavazzo [a], Pietro Asinari [a,c], Manuel Laspalas [b], Agustín Chiminelli [b,*], Matteo Fasano [a,*]

[a] Department of Energy "Galileo Ferraris", Politecnico di Torino, Corso Duca degli Abruzzi 24, Torino, 10129, Italy
[b] Materials and Components Division, Aragon Institute of Technology – ITA, María de Luna 7, Zaragoza, 50018, Spain
[c] Istituto Nazionale di Ricerca Metrologica, Strada delle Cacce 91, Torino, 10135, Italy
[d] Department of Mechanical Engineering, Mehran University of Engineering and Technology, SZAB Campus, Khairpur Mir's, 66020, Sindh, Pakistan
[e] Department of Engineering for Innovation, University of Salento, Piazza Tancredi 7, Lecce, 73100, Italy
[f] Foundation of Research and Technology-Hellas, Institute of Chemical Engineering Sciences, Stadioustr Rion, Patras, 26504, Greece
[g] RNANO Lab—Research Lab of Advanced, Composite, Nanomaterials and Nanotechnology, School of Chemical Engineering, National Technical University of Athens, 9 Heroon Polytechneiou St., Zografos, Athens, 15773, Greece

ARTICLE INFO

Dataset link: https://github.com/paolodeangelis/CGMD_PLA-Gr, https://doi.org/10.5281/zenodo.14056590

Keywords:
Nanocomposites
Multiscale modeling
Coarse-grained molecular dynamics
Polylactic acid
Graphene
3D printing
Thermal and mechanical properties

ABSTRACT

Carbon-based nanoparticles can significantly enhance the specific characteristics of polymers, impacting mechanical, thermal, electrical, and magnetic properties. However, incorporating these enhancements into final products can be challenging due to the influences of subsequent processing steps required to transform the material into components. This is the case of nano-modifications of 3D printing thermoplastic filaments. The filament characteristics and the printing process's resulting material microstructure affect the final properties of the material produced. The resulting material exhibits a hierarchical multiscale structure, necessitating a combination of various simulation approaches and methods to capture the relevant effects and influences across different scales, ultimately allowing for accurate prediction of the final material response in the product. This study focuses on predicting key thermal and mechanical properties of polymer nanocomposites and 3D printing materials. The analysis is based on coarse-grained molecular dynamics and continuum models across different scales, complemented by experimental characterization of the base material (filament) and micrographic analysis of the printed material. The findings demonstrate the potential of modeling to predict various material responses. The multiscale model reveals that with a modest addition of nanofiller (up to 2 wt%), the Young's modulus and thermal conductivity show up to 11% enhancement. These predictions closely align with the experiments, exhibiting a maximum deviation of 2.3%. In conclusion, this study demonstrates that the combination of diverse modeling techniques and experimental validation provides valuable guidance for materials development and engineering, as well as a deeper understanding of the process/structure/properties relationships.

1. Introduction

The term "additive manufacturing" encompasses a range of technologies, including Fused Filament Fabrication (FFF), Stereolithography (SLA), and Selective Laser Sintering (SLS), which enable the production of 3D solid objects from digital files through the layered deposition of materials. These technologies mark a paradigm shift in product design and manufacturing, being increasingly used in sectors such as automotive, aeronautics, medical, energy, and consumer

* Corresponding authors.
E-mail addresses: achiminelli@itainnova.es (A. Chiminelli), matteo.fasano@polito.it (M. Fasano).
[1] Shared first authorship

https://doi.org/10.1016/j.compositesb.2025.112354
Received 24 September 2024; Received in revised form 14 February 2025; Accepted 26 February 2025
Available online 10 March 2025

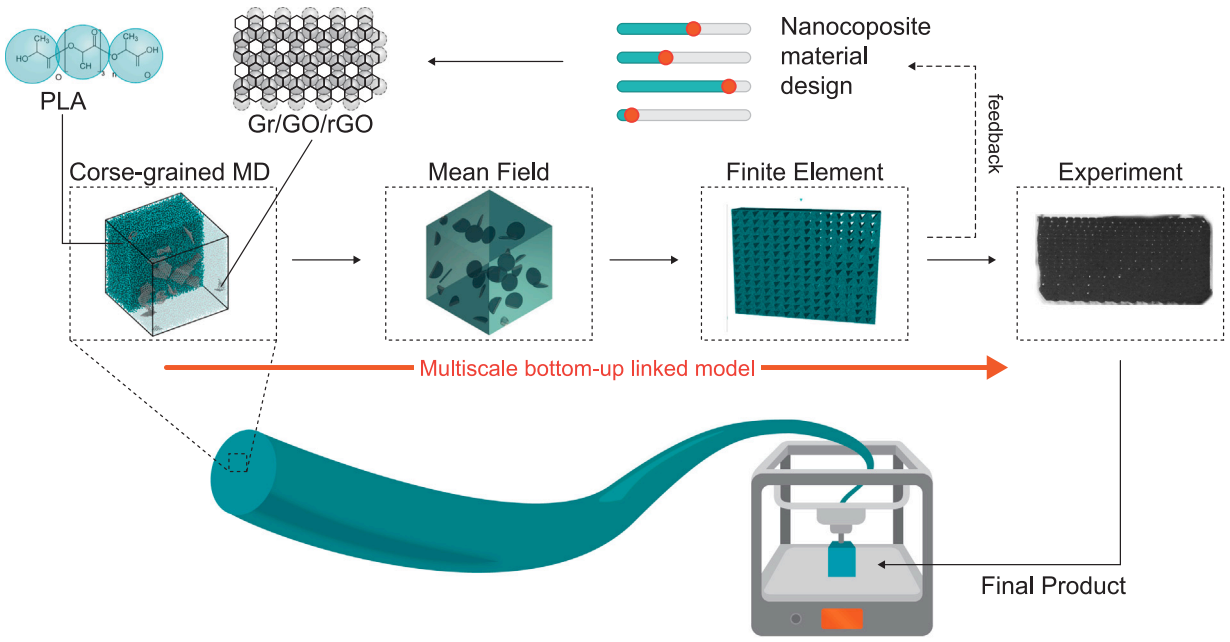

Fig. 1. Scheme of the multiscale approach employed in this work to characterize enhanced filaments for 3D printing, both *in silico* and *in operando*.

goods [1–3]. 3D printing offers advantages over conventional methods, including reduced material waste and the ability to create complex shapes without molds [4]. It allows the fabrication of intricate structures that support localized cooling requirements. For instance, Chen et al. [5] demonstrated leaf-vein-like aluminum oxide (Al_2O_3) structures embedded in epoxy (EP) matrices, enhancing thermal conductivity by up to 5585% compared to neat EP. However, limitations exist in terms of materials, properties, sizes, and post-processing requirements.

Among the various 3D printing techniques, FFF uses a continuous filament of a thermoplastic material that is extruded and deposited according to a predefined geometry [4]. The performance of the printed product will be influenced by the key processing parameters such as printing velocity, temperature, or filament diameter [4]. One of the most critical aspects in 3D printing is the proper definition of the printing parameters to avoid problems such as distortions or voids. Precise parameter definition is crucial to mitigate these defects, which continue to pose challenges and frequently compromise the strength of printed components. Numerous studies have explored the influence of different printing parameters on product quality and properties. For example, Coppola et al. [6] studied the effect of the printing temperature on PLA/clay, while Yao et al. [7] investigated the effect of the printing orientation on the ultimate tensile strength. Chacón et al. [8] analyzed the influence of the built orientation, layer thickness and feed rate. The effect of the voids was studied in detail by Tessarin et al. [9] and Tao et al. [10]. Rahmatabadi et al. [11] observed that the presence of voids and the unique morphology characteristic of PLA and thermoplastic polyurethane (TPU) blends impact the material's ability to store and release strain energy. Some authors have performed similar studies using computational tools such as parametric studies of the printing parameters [12], reduced order models [13] or probabilistic analysis [14].

The properties of 3D printing materials can be significantly enhanced through the incorporation of fillers [15], including carbon fibers, carbon nanotubes (CNTs), and graphene particles [16,17]. Various micro or nano-modified polymer products are available in the market [18,19]. Enhancing filament properties through material modification is an area of active research. For instance, Arunkumar et al. [20] investigated the influence of carbon additives on tensile, bending, and impact strengths in Polyamide (PA) and Polylactic Acid (PLA) 3D printed structures with varying filler concentration. Caminero et al. [21] studied the effect of graphene nanoplatelets on the properties of PLA FFF printing material. Aumnate et al. [22] have evaluated the production of acrylonitrile Butadiene Styrene (ABS) modified with graphene oxide to enhance the mechanical properties. Masarra et al. [23] examined PLA and Polycaprolactone (PCL) nanomodification for higher electrical conductivity.

Beyond enhancing material strength and conductivity, the use of nanofillers can also impart time-dependent responsiveness in printed objects, enabling materials to respond dynamically to thermal, electrical, or magnetic external stimuli. This adds a "fourth dimension" to traditional 3D printed structures, giving rise to 4D printing, a field focused on creating materials with programmable dynamic responses [24]. This innovative use of nanofillers expands the scope of additive manufacturing to produce functional objects for applications such as shape-memory devices, piezoelectric soft sensors, and soft robotics. For instance, Mousavi et al. [25] created a novel tactile sensor by reinforcing polylactic acid (PLA) with carbon nanotubes (PLA/CNT), introducing anisotropic structures that allow multidirectional tactile sensing. Another study by Rahmatabadi et al. [26] demonstrated the integration of Fe_3O_4 nanoparticles in polyethylene terephthalate glycol (PETG), enabling shape recovery activated by both magnetic and thermal stimuli. Even in this context, both printing parameters and the interaction between nanofillers and the polymers were thoroughly investigated to control the behavior of materials under dynamic conditions. Zolfaghari et al. [27] further analyzed the impact of printing parameters and recovery temperature on shape memory behavior in PLA blended with TPU, which provided insights into how these factors influence shape memory polymer (SMP) functionality. Rahmatabadi et al. [28] investigated the effects of blending PLA with various concentrations of polybutylene adipate terephthalate (PBAT), finding that a 30% PBAT concentration achieved an optimal balance between mechanical integrity and rapid shape recovery.

While these fillers contribute to enhanced material properties and behavior, they also modify other important aspects such as the density or the melting point. Therefore, optimizing printing parameters to ensure proper processing and achieve the desired product characteristics is essential.

A major challenge in materials science is the accurate modeling and prediction of behavior for these complex, multi-component materials [29–31]. The final properties of the printed material are influenced

not only by the filament characteristics but also by the internal material structure developed during the printing process. This yields to a hierarchical multiscale structure: nanoscale polymer modifications, microscale internal structures, and macroscale product features including potential printing defects. Each level significantly influences the final material properties. From the point of view of the material modeling, this requires a combination of different simulation approaches allowing to capture the relevant effects and influences at the different scales and, together, permitting to obtain a prediction of the final material response in the product [32,33].

In light of the aforementioned research landscape, the primary objectives of this study are to: (1) develop an *in silico* model for 3D printed PLA nanocomposites by integrating mesoscale, homogenization, and continuum methods; (2) predict the impact of various nanofillers on the mechanical and thermal properties of the material and validate these predictions through experimental characterization; and (3) assess the performance of these enhanced materials and evaluate the effects of printing-induced defects on the final 3D printed product. Specifically, we focus on PLA-based nanocomposites due to their significant technological and scientific interest [34]. PLA is a biocompatible and biodegradable thermoplastic polymer that can be obtained either from natural resources or synthetically. Due to its low production cost and minimal environmental impact compared with other materials, it has been considered for applications in food packaging, textiles, and recently as an engineering plastic [34,35]. Molecular dynamics (MD) simulations have the capability to foreknow the material properties (for example, structural and thermal properties) of polymers from their description at the atomistic level. However, these techniques are constrained by the length and time scales required for comprehensive analysis of nanocomposite properties [36]. To overcome these limitations, mesoscale models, particularly coarse-grained models, are essential. In these models, various atoms are clustered into one new united particle for which interparticle interactions are derived from the full atomistic simulations. This approach not only reduces the system's degrees of freedom but also enables the study of larger systems over extended time scales. At this scale of material description, it becomes feasible to transition to continuum modeling using analytical or computational approaches. These last models are well-suited for studying material structures at the microscopic level, including defect patterns induced during 3D printing processes.

Taking all this into account, a "multiscale bottom-up linked" [37] approach was designed to address this challenge, with performance illustrated in the following results section. This approach uniquely combines Coarse-Grained Molecular Dynamics (CGMD), mean field, and finite element methods, bridging molecular insights with continuum-level modeling to predict the thermal and mechanical properties of PLA/graphene nanocomposites for 3D printing. Unlike previous studies, which often isolate molecular or macroscopic properties, our integrated approach captures the combined influence of nanofiller characteristics, filler–matrix interactions, and the structural defects resulting from the 3D printing process on the final material properties. Our methodology employs a dedicated set of equations for each scale, with crucial parameters at each scale fed from the model at the lower scale, as depicted in Fig. 1. This multiscale framework enables a comprehensive understanding of the relationships among nanocomposite composition, 3D printing parameters, and final product properties, directly addressing a critical gap in current understanding.

In our protocol, we begin by developing a mesoscopic model of neat PLA using the Martini Coarse-grained force field [38]. The PLA system was modeled through CGMD simulations and then the curve of density of material versus temperature acquired to determine the glass transition temperature. Subsequently, we analyze the PLA system to determine key thermophysical properties, including Young's modulus, Poisson's ratio, specific heat capacity, and thermal conductivity. Next, we develop CGMD models for various fillers: graphene (Gr), graphene oxide (GO), and reduced graphene oxide (rGO). The results of the coarse-grained simulations were compared to published mesoscopic results. We then assess the impact of these fillers on the thermophysical properties of PLA. Finally, to verify our CGMD model of PLA/Gr nanocomposites, we compare its predictions against those of continuum Finite Element (FE) and Mean Field (MF) models. For further validation, we conduct experimental characterization of elastic constants and thermal conductivity for both PLA and PLA/Gr nanocomposites. In all cases, different graphene particles concentration have been evaluated. Lastly, we develop another FE model to evaluate the material properties of 3D printed structures. The homogenized thermal and mechanical properties of a 3D printed material were estimated using the properties obtained from the CGMD models and the internal structure of a real printed sample.

In Section 2, we detail all the technical aspects of the models and experimental setups. The protocol's results are presented in Section 3, followed by the conclusions and a discussion on the future outlook in Section 4.

2. Methods

This section provides a comprehensive overview of the technical details underlying our study's methodology. We begin by outlining the multiscale protocol, detailing the physical phenomena at different scales and the derivation of the corresponding material properties. Next, we describe the experimental techniques used to characterize the nanocomposite material and the 3D-printed samples that validate our model predictions.

2.1. Multiscale protocol and experimental characterization of nanocomposite filament

The PLA filament studied is a blend of the polymer with various types of graphene-based nanoparticles at different concentrations. Modeling such composites necessitates a clear definition of the constituents. Depending on the approach, this can be achieved through dedicated models for each phase or material, or via experimental methods.

In this work this has been done through dedicated CGMD models for both the PLA matrix and the graphene fillers (Gr/GO/rGO). These models were subsequently integrated into nanocomposites CGMD model.

To verify the results obtained for the nanocomposite, we compared them with MF and FE simulations, which serve as continuum models for the PLA/Gr composite. Additionally, an experimental campaign was conducted to validate the model and the underlying hypotheses associated with the specific graphene filler used.

2.1.1. Coarse grained model

The Martini force field was employed to model the intermolecular and intramolecular interactions in PLA, where each PLA molecule ($C_3H_4O_2$) was represented by a single bead. In the CGMD model of graphene and graphene oxide, three to four atoms are clustered into a single bead, simplifying the representation of these materials. The models contain bonded and non-bonded interactions. Bonded interactions consist of bonds, angles, and dihedrals, whereas the non-bonded interactions are defined by the 12–6 Lennard-Jones (LJ) potential. The 12–6 LJ potential is also adopted to simulate van der Waals forces that contribute to the interfacial adhesion between the polymer matrix and nanofillers. A detailed description of the formulations and parameters for both bonded and non-bonded interactions for each phase is provided in a dedicated Section S2 of the supplementary material.

To conduct the simulations, a structured data file defining the structure of the materials and an input file containing the information of the force-field parameters, conditions and commands are needed. In this work, the data file for CGMD model of PLA was constructed using the `Mc_gen` software developed by Tschopp and Ward [39]. The CGMD PLA model was thus obtained defining the chain length (150 beads in

a single chain of PLA), the number of chains (400), the bond length (0.434 nm) and the molecular weight of the PLA bead (72.06 g/mol).

The data file of graphene for CGMD simulation has been created using Visual Molecular Dynamic (VMD) [40], where the atomic bond length (0.142 nm) for carbon–carbon (C–C) interactions was adjusted to match that of the CGMD model for graphene (0.248 nm). For the initial structure of graphene oxide and reduced graphene oxide, a custom C++ code was developed to facilitate the necessary modifications, as detailed in the supplementary material file (Section S4). The composite systems of PLA with varying weight fractions of graphene, graphene oxide, and reduced graphene oxide were constructed using the "`fix deposit`" command from the LAMMPS (Large-scale Atomic Massively Parallel Simulator) [41] package. This method randomly places nanofillers throughout the simulation box, with each nanoparticle also undergoing a random rotation around its center of mass to simulate a realistic nonuniform distribution.

All the CGMD molecular dynamics simulations for the PLA, the graphene and the composites were carried out with the code LAMMPS. The control of pressure and temperature was done through the Nose–Hoover barostat and thermostat [42,43] with relaxation constant τ of 0.1 ps and 1 ps respectively. The Verlet algorithm was employed to integrate the equations of motion, with a time step of 1 fs. Prior to computing the thermophysical properties, the models underwent an initial energy minimization procedure. Next, the models were equilibrated in a constant number of atoms, volume and temperature (NVT) ensemble at 500 K for 1 ns. The simulation box was then compressed in a constant number of atoms, pressure and temperature (NPT) ensemble at 5 atm and 300 K for 1 ns. Finally, the models were further equilibrated in an NPT ensemble at 1 atm and 300 K for 15 ns. Supplementary Figure S1 shows an example of the box used for the PLA, composed of 60 000 beads containing 400 chains, with each chain having 150 repetitive units. The specific protocols to be followed depend on the property being characterized, as outlined below.

i. Density and glass transition temperature (T_g). The glass transition temperature is a key physical property of polymeric materials, defining whether they exhibit glassy or rubbery behavior and influencing their processing and operational temperature range. In the CGMD simulations conducted, T_g was determined by observing changes in density or specific volume as a function of temperature. This method leverages the distinct linear relationships between density and temperature above and below T_g. Thus, after equilibrating the coarse-grained model of PLA, the glass transition temperature was determined by recording the density at various temperature conditions applied during NPT equilibration. Specifically, the equilibration process involved gradually increasing the temperature from 280 K to 400 K in 10 K increments. Using the densities obtained from the equilibrated model at different temperatures, the glass transition temperature was computed by analyzing the discontinuity in density as a function of the temperature profile.

ii. Mechanical properties (E and ν). Mechanical properties, including Young's modulus (E) and Poisson's ratio (ν), were characterized. In CGMD simulations, uniaxial deformation was applied to the system independently along the three principal directions (x, y, and z), and the mechanical response was recorded. For unidirectional tension, strain was applied along one direction at a time, and the procedure was repeated for the other two directions using the same undeformed structure. The elastic behavior of the molecular systems was interpreted using continuum mechanics. These deformation processes were performed in an NVT ensemble at a temperature of 300 K.

The deformation process obeys the Hooke's law [44]:

$$\boldsymbol{\sigma} = C\boldsymbol{\varepsilon}, \tag{1}$$

where $\boldsymbol{\sigma}$ is the stress vector, $\boldsymbol{\varepsilon}$ is strain vector and C is the stiffness matrix. Polymers are considered as isotropic materials, which means that material properties are constant in each direction. Isotropic materials are characterized by two independent variables (elastic constants) in their stiffness and compliance matrices, while anisotropic materials possess 21 elastic constants. For the isotropic case, the two elastic constants are Young's modulus E and the Poisson's ratio ν [44]:

$$\begin{bmatrix}\varepsilon_{11}\\ \varepsilon_{22}\\ \varepsilon_{33}\\ \varepsilon_{23}\\ \varepsilon_{13}\\ \varepsilon_{12}\end{bmatrix} = \frac{1}{E}\begin{bmatrix}1 & -\nu & -\nu & 0 & 0 & 0\\ -\nu & 1 & -\nu & 0 & 0 & 0\\ -\nu & -\nu & 1 & 0 & 0 & 0\\ 0 & 0 & 0 & 1+\nu & 0 & 0\\ 0 & 0 & 0 & 0 & 1+\nu & 0\\ 0 & 0 & 0 & 0 & 0 & 1+\nu\end{bmatrix}\begin{bmatrix}\sigma_{11}\\ \sigma_{22}\\ \sigma_{33}\\ \sigma_{23}\\ \sigma_{13}\\ \sigma_{12}\end{bmatrix}. \tag{2}$$

For unidirectional tension, a small axial strain rate (1×10^{-7} nm/fs = 1 mm/s) was applied on the simulation box while the other strain components remain at zero. Hence the Poisson ratio and elastic modulus was calculated for each direction and averaged values were taken.

iii. Thermal conductivity (λ). To investigate the thermal conductivity, a Müller-Plathe method [45] based on non-Equilibrium Molecular dynamics simulations is used. This non-equilibrium MD (NEMD) method involves setting up two cold regions at opposite ends of simulation box. A heat flux is then imposed at middle region (hot section) thus inducing the temperature gradient in the model. Velocities exchange between the atoms of hot and cold region generates heat flux. The periodic boundary conditions (PBC) were applied in x, y, and z directions. Once the system reaches a steady state, the amount of energy per unit time and cross-sectional area transferred from the hot region to the cold region by the exchange of velocities between molecules can be determined using the following equation [46]:

$$j = \frac{1}{2tA}\sum_{transfers}\left[\frac{m}{2}\left(v_{hot}^2 - v_{cold}^2\right)\right], \tag{3}$$

where j represents the heat flux, t is simulation time, A is cross-sectional area normal to the heat flux direction, m is mass, v_{hot} and v_{cold} are the velocities of the defined atoms. The factor of 2 is due to the energy flow from the hot region to cold region in two directions. Using the heat flux and temperature gradient, thermal conductivity can be obtained using the expression of Fourier's law [46]:

$$\lambda = -\frac{\boldsymbol{j}}{\nabla T}. \tag{4}$$

iv. Specific heat capacity (c_p). Specific heat capacity is defined as the amount of heat required by a material of unit mass to raise its temperature by one degree [47]. It is a fundamental property used to describe the thermophysical and thermodynamic behavior of a material system [48]. Thermodynamic properties such as enthalpy, entropy, and Gibbs free energy, are closely related with specific heat [49], which are derived from atomic vibrational motions within molecular structures. Specific heat is typically described at either constant pressure c_p or constant volume c_v. In this study, we determined the specific heat capacity of the models at constant pressure. To achieve this, we measured the average enthalpy and temperature across a range of temperatures: from 280 K to 350 K for pure PLA, and from 280 K to 345 K for graphene. The averaged enthalpy was then plotted against the average temperature, resulting in an enthalpy–temperature plot. Finally, the c_p of material was determined from the slope of a linear fit of enthalpy–temperature curve.

2.1.2. Continuum models for nanocomposite properties prediction

In addition to the coarse-grained analysis, continuum models were employed to predict the thermal and mechanical behavior of the nanocomposites at the macroscopic level. Two types of continuum scale models were utilized in this study: the mean field model and the finite element method. The MF homogenization approach is based on the first-order Mori–Tanaka method [50], which does not require a Representative Volume Element (RVE) model or meshing. RVE models for PLA/Gr nanocomposites were developed to facilitate FE analysis. To

achieve a comprehensive continuum model that accounts for matrix–filler interactions and thermal boundary resistance, the interphase Mori–Tanaka MF (iMF) and FE (iFE) models were employed. In this model, the interphase is conceptualized as a distinct coating surrounding the nanofiller, with its thickness precisely defined at 0.5 nm, a value derived from mesoscopic simulations. Within the framework of the micromechanical model, the interphase significantly contributes to the enhancement of the composite's elastic modulus, thereby improving its mechanical integrity. In the thermal model, the interphase plays a crucial role as a thermal boundary resistance, modulating heat transfer across the interface with the surrounding matrix. The dual functional role of the interphase — both in mechanical reinforcement and thermal regulation — substantially influences the overall material properties, making it an essential factor in predicting the effective thermal and mechanical behavior of the composite material. In the FE method, the RVE consists of a PLA matrix with graphene particles included as platelet-like shapes, assuming a perfectly bonded interface with an aspect ratio of 10, as shown in supplementary Figure S5, and similar to that used CGMD model. The mesh type used for the FE analysis was conforming tetrahedral with quadratic elements, incorporating internal coarsening and curvature control. Periodic boundary conditions were applied to the RVE models to ensure an accurate simulation of the material's bulk behavior.

FE models calculated the thermal conductivity of nanocomposites by numerically solving Fourier's law of conduction. These models also served to understand the macroscale mechanical properties of nanocomposites by simulating mechanical tests. The constituents of the RVE were assumed to be isotropically symmetric within the nanocomposite, with the constitutive relation described by generalized Hooke's law. Both approaches mentioned (MF and FE) were employed to evaluate the Young's modulus, Poisson's ratio, and thermal conductivity of the models. The RVE model was generated by assigning different mass fractions (0.5 wt%, 0.8 wt%, 1.0 wt%, 1.5 wt%, 2.0 wt%) to study the different fillers concentrations and considering a random distribution of inclusions.

2.1.3. Nanocomposite experimental characterization

To experimentally characterize the mechanical properties of PLA and PLA/GNPs nanocomposites, a thermomechanical testing campaign was conducted. For sample preparation, Polylactic Acid polymer was supplied by PrimaValue and used as filament for 3D printing. The specific properties of the filament include a density of 1.03 g/cm^3, a material flow rate (MFR) of 8.0 g/min at 220 °C for 10 kg, a diameter of 1.75 mm, melting temperature of 210 ± 10 °C, and melting point range 145–160 °C [51].

The production of graphene nanoplatelets was carried out using a commercially available shear laboratory mixer from Silverson. The resulting size distribution of the graphene platelets is presented in supplementary Figure S9. The raw material for the production process was graphite powder obtained from NGS Naturgraphit GmbH, Germany, with an average particle lateral size of 500 μm. The main component of the mixing apparatus is a 4-blade rotor placed within a fixed screen (stator), which applies the necessary shear stress for graphite exfoliation.

After weighing the graphite powder into the mixing vessel, an aqueous-based exfoliating liquid containing surfactant (Triton-X) was added. During the initial stage of the shear exfoliation process, the mixer head is submerged in the liquid solution and operates at a low rotational speed. The speed is gradually increased from 1000 rpm to 5000 rpm, and the system runs at high speed for approximately 40 min. Finally, the mass of the produced exfoliated graphene is measured after drying at 80 °C for 24 h under vacuum conditions.

The carbon content of the produced graphene nanoplatelets is approximately 91%. The GNPs powder was dispersed on adhesive conductive tape for scanning electron microscope (SEM) characterization, as shown in Fig. 2. The platelets exhibit a lateral dimension within the range of 2–5 μm and a thickness of 5–7 nm. The material appears to be partially exfoliated or reaggregated, with some platelets showing highly exfoliated regions alongside thicker crystals.

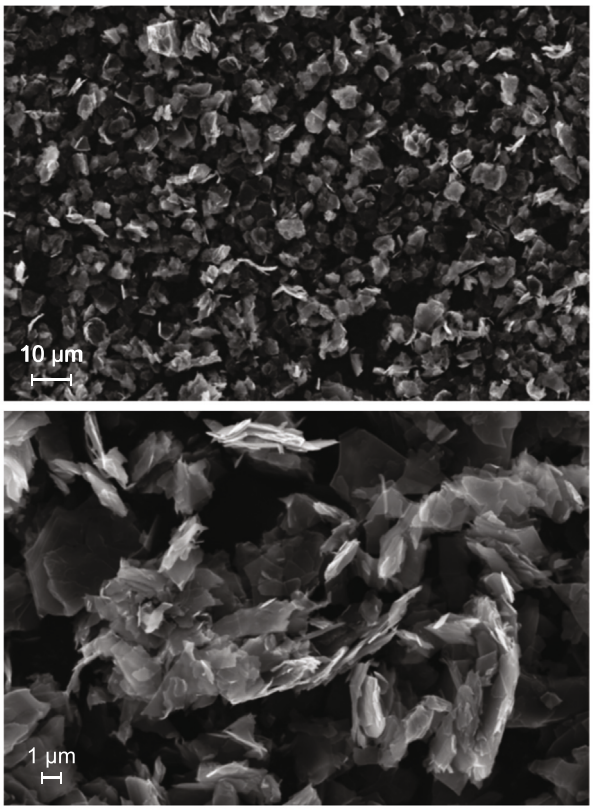

Fig. 2. SEM images of graphene nano-platelets, at different magnifications (IMM-CNR Bologna, Italy). CC-BY 4.0 [32].

PLA containing 0, 0.5, 1.0 wt% of the graphene were prepared by means of the hot press. For preparation of the polymeric film of PLA, we took around 15 g of PLA and heated them at 210 °C using hot press for around 5 min, then pressed at high pressure of 30 bar. The procedure was followed ten times to get homogeneous material. Films, after heating and pressing, were taken out from the hot press, and then quenched in the ice to get amorphous structure and prevent crystallization. Amorphous polymers are generally preferred due to their enhanced processability, faster production rates, and isotropic properties. A similar procedure was applied to the PLA/Gr composite, with the addition of a melt premixing step to incorporate nanoinclusions into the PLA matrix at concentrations of 0.5 and 1.0 wt%.

Specimens of PLA, PLA/GNPs were prepared using ASTM international standard test method for tensile properties of Plastics (ASTM D882-02 [52]). They were machined into 100 × 10 mm^2 rectangle specimens. Thickness of these samples were taken at various length and the average value recorded, then the area of each strip was calculated to determine the stress acting on the strips. Specimens were tested in mechanical tensile system (MTS) at room temperature with the strain rate of 25 mm/min as illustrated in Fig. 3. Five test repetitions for each composition were done at 300 K, and average values of Young's modulus were obtained.

To investigate the thermal conductivity of pure PLA and PLA/GNPs (0.5 and 1.0 wt%) composites, test specimens were prepared in a rectangular shape with dimensions of 30 mm in length, 30 mm in width, and 5 mm in thickness. Two samples of each configuration were prepared, and repeated measurements were performed five times for each sample.

Thermal property measurements were conducted on the PLA and PLA/Gr composite samples using the transient plane source (TPS)

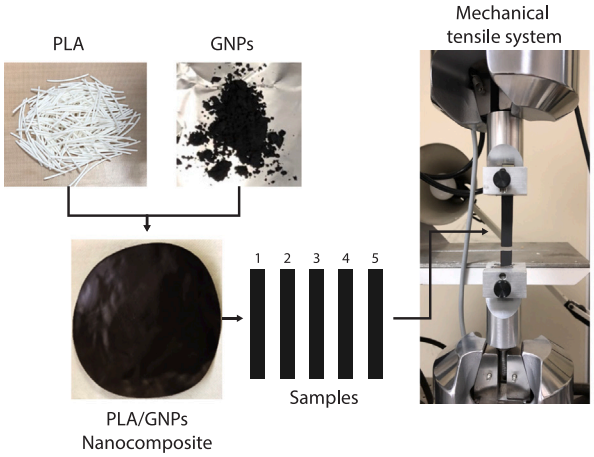

Fig. 3. Experimental protocol for the mechanical characterization of PLA/GNPs composite.

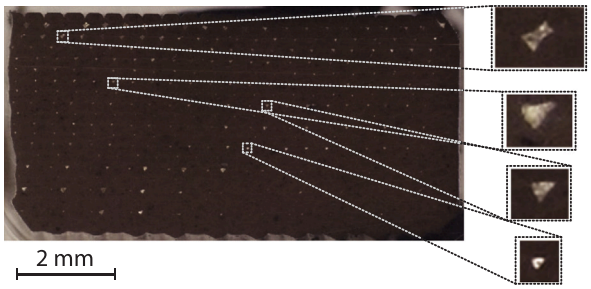

Fig. 4. Section of the 3D printed sample prepared for analysis, showing examples of the triangular and rhomboidal defects resulting from the printing process.

Table 1
Dimensions of the triangular defects.

	Area (mm^2)	a (mm)	b (mm)	c (mm)	θ (°)
Triangle M (i)	0.095	0.003	0.063	0.023	6.936
Triangle L (ii)	0.176	0.011	0.125	0.049	12.98
Triangle S (iii)	0.095	0.001	0.0364	0.0133	6.936

method and the Hot Disk thermal constants analyzer at room temperature (≈25 °C). This investigation adhered to the guidelines outlined in the international standard ISO 22007 [53] for both the TPS method and the Hot Disk instrument.

In this study, the sensors were carefully positioned between the planar surfaces of two sample pieces of the material under investigation. The Hot Disk sensor, which comprises a double spiral electrically conductive pattern etched into a thin nickel sheet, played a pivotal role in the measurements. The fundamental principle of the experimental setup involved providing a continuous power supply to the initially isothermal sample through the Hot Disk sensor.

Subsequently, the same sensor functioned as a resistance thermometer to monitor the resulting temperature rise over a defined heating period. Throughout the experimental procedure, the dynamic characteristics of the temperature rise were meticulously recorded and analyzed by examining the corresponding changes in sensor resistance. This analysis allowed for the determination of both thermal conductivity and thermal diffusivity from a single transient recording.

2.2. Modeling and experimental characterization of final 3D printed material

Following the previously described workflow, the second part of the study focused on analyzing the thermal and mechanical properties of the 3D printed material. These properties are crucial for the analysis and design of components made from these materials, integrating the effects of polymer nano-modification and the manufacturing process. The microstructure plays a significant role in determining the properties studied, necessitating an *ad hoc* approach to characterize the geometrical aspects of the internal structure. To achieve this objective, a FE model of a RVE of the 3D printed material was developed. This model considered the internal structure characterized from a real sample, allowing for a more accurate representation of the material's behavior. In this section, we present a comprehensive report on the methodology and standards followed to complete the multiscale protocol, culminating in the final product properties prediction and experimental validation.

2.2.1. 3D printing material characteristics extraction

Due to the manufacturing process, void channels appear between filaments, resulting in an anisotropic material with different properties along its directions (see Fig. 4). The material system used in this characterization focused initially on pure PLA. The sample was fabricated and sliced to enable the acquisition of images using optical microscopy. Specifically, the specimens manufacturing was done using a "Raise3D Pro 2 Plus FFF" system, with the printing parameters detailed in supplementary Table S8. An example of one of the sections obtained from the sample is shown in Fig. 4, providing a visual representation of the internal structure produced by the 3D printing process.

As observed, the defect pattern is not uniform across the section, with varying sizes and shapes of defects present. Additionally, the defects are not evenly distributed throughout the material. This phenomenon can be attributed to manufacturing conditions such as deposition velocity and filament thickness.

To gain further insights, a surface analysis was performed using the software ImageJ [54,55]. The analysis reveals that the global porosity of the studied section is approximately 0.87%, although different areas exhibit variable porosity levels.

The geometry and dimensions of the defects were analyzed, revealing that most defects have a triangular shape; however, some rhombus-shaped defects were also observed and characterized (see supplementary Figure S6 for additional information on geometry control). Furthermore, the distances between defects were also determined. The parameters used to characterize each shape and the defect area were measured using ImageJ [54,55].

As observed in Fig. 4 (right), different defect geometries are created depending on the location within the section. To evaluate the effect of the observed defect morphology, four cases were studied:

i An average triangular defect obtained from two defects (Triangle M).
ii A large triangle derived from the lower part of the section, characterized by larger distances between defects (Triangle L).
iii A triangle similar to that in case (i) but representing the most frequently occurring area (Triangle S).
iv The same average triangle as in case (i), but with a shift applied to every second line equal to half the triangle's step (Triangle Alt.).
v An irregular rhombus obtained from the upper part of the section (Rhombus).

The software used can provide a list of defects and their sizes; however, due to the small dimensions of some defects, manual measurement is not feasible. Therefore, the triangle in case (iii) is considered proportional to case (i), scaled to represent the most frequently occurring area. This area has been determined to be $0.001\ mm^2$. The exact dimensions of the triangular and rhombus defects are included in Tables 1 and 2.

The distances between consecutive defects in the vertical and horizontal directions (see Fig. 12.a) have been estimated to define the

Table 2
Dimensions of the rhombus defects (iv).

a (mm)	b (mm)	c (mm)	α (°)	β (°)	γ (°)
0.05	0.09	0.05	53.97	39.81	48.58

defects distribution. The average horizontal distance is 0.366 mm, while the average vertical distance is 0.212 mm. However, it is observed that in the lower left part of the section, where defects of type (ii) are found, the defects are larger, and the separation between them is greater. Consequently, in this zone, the horizontal and vertical distances are approximately twice the average values. In future studies, this image processing approach could be improved using artificial intelligence methodologies, allowing faster extraction and averaging of information from larger samples/areas [56] and transfer to models.

2.2.2. Continuum model for 3D printing material properties prediction

A Python script was implemented to automatically generate the model geometry with the desired number and shape of defects. RVEs were created considering the defect geometries presented in Fig. 12.a. The RVEs consist of regular 3D structures, including 10 defects along each direction, except for configuration (ii), which, due to the separation between defects, includes 5 defects in each direction. The dimensions of the RVEs are 3.66 mm×2.12 mm×0.2 mm. The volume must be meshed such that the meshes on parallel faces coincide, allowing for the application of the periodic boundary conditions defined in the next section. To verify that the mesh refinement is adequate for accurate simulations, a mesh sensitivity analysis was conducted. Coarse and fine mesh configurations were compared (supplementary Figure S8), showing a difference of less than 1% in the estimated mechanical and thermal properties (see supplementary Table S10 and Table S11). This confirms that the coarse mesh provides sufficient accuracy for our analysis. Heat transfer elements (6-node linear triangular prism and 8-node linear brick [57]) are employed in the thermal analysis, while stress elements (4-node linear tetrahedron and 8-node linear brick [57]) are used in the mechanical analysis. A total of five structures were simulated. In four of them the defects are evenly distributed creating a regular grid and in the last one defects of type (i) are in alternated positions on each printing plane (Fig. 12.a).

The procedure to estimate the thermal and mechanical properties of the printed material consists of a homogenization analysis with some particularities in each case. The homogenized properties are obtained using the Micromechanics Plug-in for Abaqus/CAE [58]. The homogenization process involves the three following steps.

In the first step, the model is built, and loads and boundary conditions are defined using the Micromechanics Plug-in. PBC are imposed on the RVE to ensure that it is representative of a larger material volume. This means that the RVE repeats periodically in all three spatial directions, and the conditions on parallel faces are identical. An example of a possible RVE of the printed material is presented in supplementary Figure S7. The plug-in imposes a relationship on the boundary nodes of the RVE using equation constraints. These relationships can be in terms of displacements to obtain the mechanical properties or temperatures to obtain the thermal conductivities. A reference node, to which the load is applied, is defined, and parallel faces of the RVE are related to the load node through the equations. PBC require nodes to be positioned periodically to impose the periodic equations.

A solution field, φ, with periodic response exhibits the form [59]:

$$\varphi\left(x_i + p_j^{\alpha}\right) = \varphi\left(x_i\right) + \left\langle \frac{\partial \varphi}{\partial x_i} \right\rangle p_j^{\alpha} \tag{5}$$

where x_j is the coordinate, p_j^{α} is the αth vector of periodicity, and $\langle \partial\varphi/\partial x_i \rangle$ is the far-field gradient of the solution field.

Thermal loads are defined using three load cases corresponding to three temperature gradients imposed between parallel faces of the RVE. These temperature gradients induce thermal fluxes between parallel faces.

Mechanical loads are defined using six load cases corresponding to six imposed deformation modes, according to the normal and shear directions.

In the second step, the analysis is solved using Abaqus [60]. The load cases are executed sequentially, simulating heat fluxes (thermal analysis) or deformations (mechanical analysis) along the three directions. The final step involves post-processing the results with the Micromechanics Plug-in to obtain the homogenized material response. The thermal conductivities are determined by applying Fourier's Law (see Eq. (4)).

It is possible to select the desired material type that better fits the homogenized material. In the analysis here presented the analyzed material has been considered orthotropic (transversely isotropic), defined by the directional thermal conductivities, λ_{11}, λ_{22} and λ_{33}.

Similarly, the mechanical behavior of the material can be characterized according to different material models. In this work, the material is characterized by its elastic properties, specifically the elastic modulus, Poisson's ratio, and shear modulus. Then, the anisotropy is only due to the internal material structure produced by the 3D printing process. More complex constitutive models could be used to perform further analysis, for example trying to reproduce non linear behaviors or other effects as anisotropy due to reinforcement reorientations [61,62].

3. Results

In this section, we present the results of the multiscale bottom-up linked model developed to predict the properties of composite filaments for additive manufacturing. The evaluation begins with the thermal and mechanical properties of the individual matrix and filler components. The influence of these fillers on the overall material properties is assessed at the mesoscale. These key parameters are then used in a continuum model to investigate the impact of the microstructure on the filament and the final printed product. Following the intrinsic hierarchical structure of the problem, we begin with the mesoscale evaluations and progressively move to the continuum models and experimental validations.

3.1. Mesoscale

3.1.1. Polylactic Acid (PLA)

The coarse-grained model of PLA, illustrated in Fig. 5.d, reduces the degrees of freedom of the atomistic model, enabling efficient modeling of relatively large simulation boxes. To assess the effectiveness and limitations of this coarse-grained approximation, we computed several key macroscopic quantities.

By simulating the system in an NPT ensemble with varying temperatures from 280 K to 400 K and a constant pressure of 1 atm, we observed that the density ranged from 1.14 g/cm^3 to 1.19 g/cm^3. These values are consistent with literature reports, which indicate that PLA density ranges from 1.13 g/cm^3 to 1.195 g/cm^3 [63]. Through this initial simulation campaign, the glass transition temperature (T_g) of the polymer was determined. As shown in Fig. 5.a, the density exhibits a significant change in slope with increasing temperature. By splitting the data into two sets at a threshold temperature and fitting each set with a straight line to minimize residuals, we estimated the T_g. For our model, T_g was found to be between 330 K and 332 K, consistent with both fully atomistic simulation and experimental values (333 K) [63,64]. This property is strongly related to the relative arrangement of the chains and van der Waals interactions [65], indicating that the CGMD model adequately captures the internal chains mobility and binding interactions. These findings validate the CGMD model's accuracy in predicting the structure arrangement and intramolecular properties of PLA, which is crucial for the further analysis.

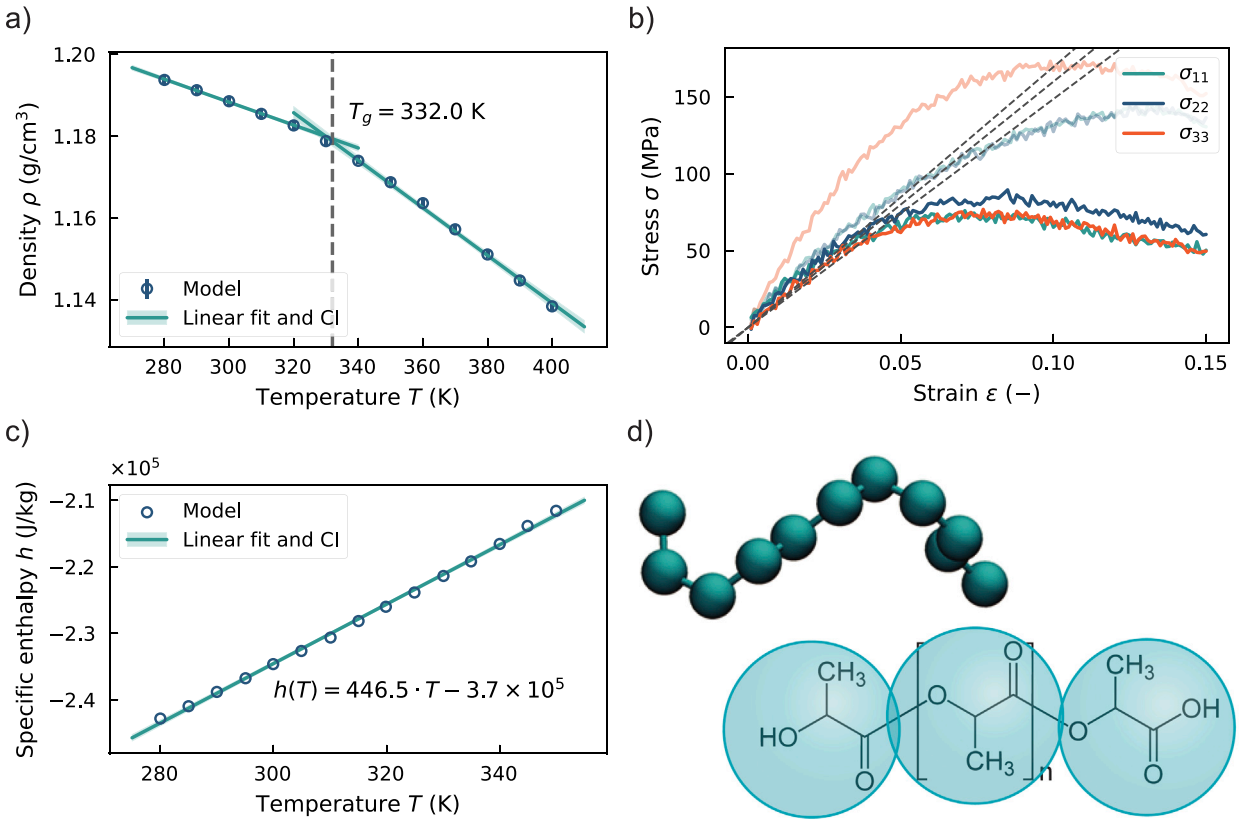

Fig. 5. Coarse-grained model predictions for pure polylactic acid (PLA) polymer. (a) Glass transition temperature predicted by identifying the slope change point in the temperature-density curve, using linear fitting ($R^2 = 99.9\%$ for $T \leq T_g$, $R^2 = 99.7\%$ for $T > T_g$,). (b) Stress–strain plot showing the three normal stress components from an axial tensile test along the x, y, and z directions. The shaded line represents the direct stress measurement for the simulation for deformation along the z direction; solid lines are corrected curves from the compliance matrix formulation, and dashed lines show ideal elastic behavior. (c) Enthalpy–temperature plot with linear interpolation ($R^2 = 99.8\%$) to compute isobaric specific heat capacity (c_p), with shaded area showing the 95% confidence interval (CI). (d) The PLA coarse-grained model, illustrating the atoms represented by each bead.

The CG model's investigation continued with a detailed study of the mechanical properties of PLA. Specifically, we computed Young's modulus and Poisson's ratio of PLA by applying a progressive deformation to the simulation box along the three principal tensile directions. This induced a one-dimensional strain on the polymer, denoted as ε_{11}, ε_{22}, and ε_{33} for the tensile tests along the x, y, and z directions, respectively.

However, due to the simulation setup and the box size, applying uniaxial strain resulted in significant deformations along the other two dimensions because of section reduction. This caused observable strains, ε_{11}, ε_{22}, in addition to the imposed one (ε_{33}), as shown by the shaded line in Fig. 5.b. Consequently, the resulting stiffness matrix contained off-diagonal components. As depicted in Fig. 5.b, the shaded line indicates the stress measured while applying ε_{33} to the simulation box, clearly showing that the stresses measured along the orthogonal directions are not negligible. By measuring the slope of the linear fit to the stress–strain curve obtained from the simulation within the strain region $\varepsilon \in [0.0, 0.05)$, where the material exhibits ideal elastic behavior (Fig. 5.b), the elastic constants C_{31}, C_{32}, and C_{33} were calculated. To accurately determine Young's modulus E and Poisson's ratio ν, we solved the compliance matrix formulation after computing all the elastic matrix components, as previously detailed in Section 2.1.1 of the Methods. This procedure allowed us to convert the three-dimensional stress state from the simulation to a one-dimensional equivalent, as illustrated in Fig. 5.b by the new stress–strain curves.

After applying this correction, the Young's modulus for the PLA phase was determined to be 1.6 GPa, which falls within the literature range of 0.35 GPa to 3.5 GPa [66]. This value also aligns well with our experimental measurement of 1.80 GPa, resulting in a deviation of approximately 11%. The Poisson's ratio was found to be 0.38, which is in good agreement with experimental values around 0.36 [66]. These results further demonstrate the accuracy of the CGMD model, which correctly describes the interactions between the PLA molecules and their tangled structure.

Following the validation of mechanical properties, thermal properties were analyzed to complete the characterization of the PLA model. We computed the thermal conductivity (λ) of PLA using the Müller-Plathe algorithm [45]. The method imposes a thermal flux, consisting in the exchange of kinetic energy between particles and thus generating a temperature gradient. By applying Fourier's law, we obtained a value of 0.112 W/(m K). This value is in agreement with the literature measurements where λ ranges between 0.13 W/(m K) and 0.19 W/(m K) [67–70], but it is 44% lower than our experimental value (0.205 W/(m K)). Possible reasons for the discrepancy include variations in sample preparation, morphological changes in the test specimens, measurement techniques, or intrinsic material properties due to processing conditions. Additionally, as noted in the literature [32], in CGMD models, groups of atoms are clustered into single beads, significantly reducing the degrees of freedom (DOF). This reduction allows for larger time steps and the simulation of larger systems, facilitating connections between computational predictions and experimental observations. However, the reduced DOF at the CGMD level can impact the accuracy of thermal property predictions, which are based on phonon transfer, at atomic or quantum scales. Consequently, capturing phonon-driven thermal phenomena remains a challenge with CGMD.

Additionally, the specific heat capacity (c_p) of CGMD PLA was computed by measuring the rate of change of enthalpy with varying system temperatures using an NPT ensemble. In the temperature range of 280 K to 350 K, we observed a linear increase in enthalpy, as shown in Fig. 5.c. By interpolating the enthalpy measurements at each temperature, we obtained a specific heat capacity of 446.5 J/(kg K). This value

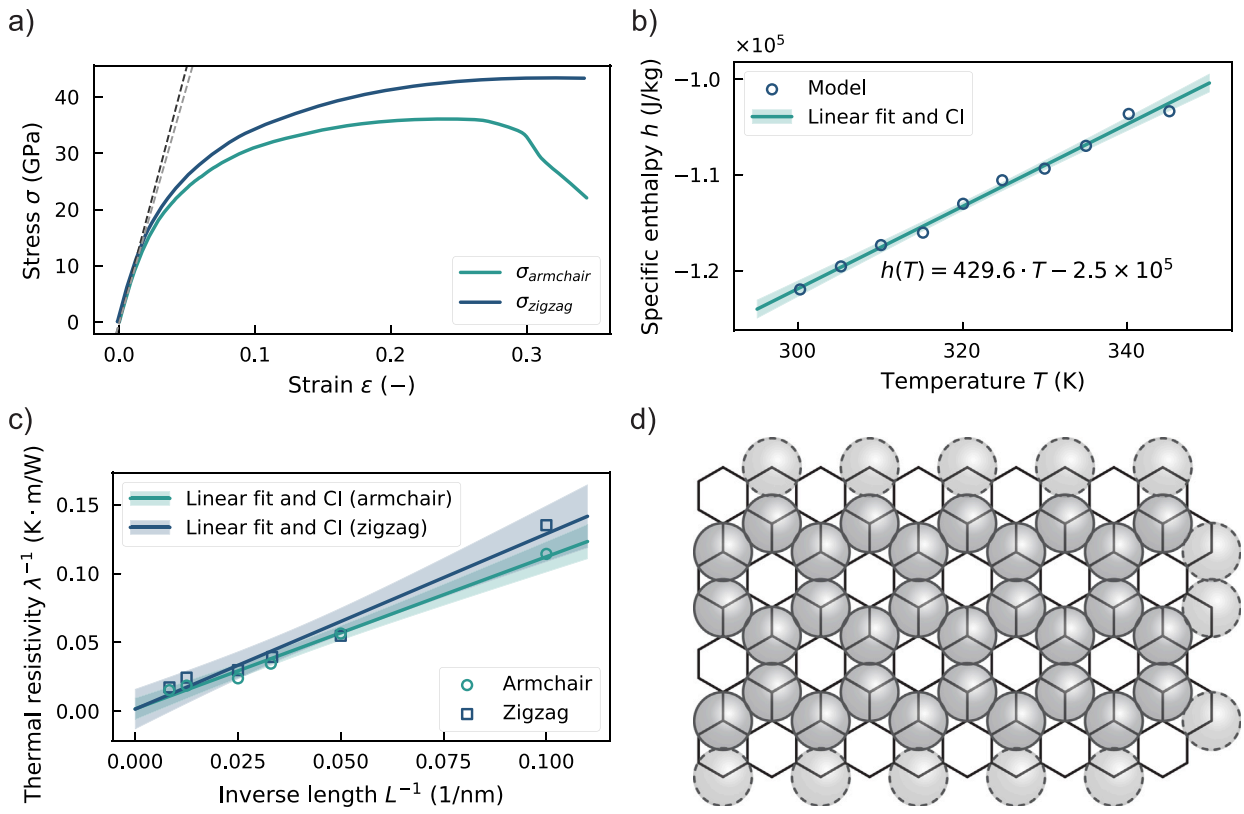

Fig. 6. Coarse-grained model predictions for pure graphene sheets. (a) Stress–strain plot showing normal stress components from axial tensile tests along the zigzag (σ_{zigzag}) and armchair ($\sigma_{armchair}$) directions, with dashed lines indicating the interpolated ideal elastic behavior for Young's modulus derivation. (b) Enthalpy–temperature plot with linear interpolation ($R^2 = 99.2\%$) and 95% CI for computing isobaric specific heat capacity (c_p) (c) Resistivity vs. inverse length plot showing the ballistic-to-diffusive transition in thermal conductivity, with the linear interpolation ($R^2 = 98.9\%$ for armchair and $R^2 = 97.3\%$ for zigzag directions) used and 95% CI shaded; cyan and blue lines represent armchair and zigzag directions, respectively. (d) Coarse-grained Gr model, with each bead representing four carbon atoms, preserving the hexagonal structure. (For interpretation of the references to color in this figure legend, the reader is referred to the web version of this article.)

is significantly lower than the experimental value of $1800\,\mathrm{J/(kg\,K)}$ at room temperature [70]. The significant discrepancy is primarily due to the DOF reduction introduced by the Martini force field employed in the coarse-grained model, which neglects the internal kinetic energy exchange of the atoms present into each larger bead of the CGMD PLA molecule [32].

3.1.2. Graphene-based fillers (Gr/GO/rGO)

Fig. 6.d illustrates the coarse-grained model of graphene (Gr). In this model, the atoms at the vertices of the hexagonal lattice and their three bonded atoms form the beads of the CGMD model [71]. This approach ensures that each bond in the CGMD model substitutes for two covalent C–C bonds, thereby preserving the hexagonal structure. The CGMD model was generated using Visual Molecular Dynamics (VMD) [40]. The construction of the structure involved changing the C–C bond length from $0.145\,\mathrm{nm}$ to $0.280\,\mathrm{nm}$, as described in the atomistic-to-coarse-grained mapping strategy, Fig. 6.d, detailed in Section S2 of the supplementary material. The final graphene sheet size was set to $20\,\mathrm{nm} \times 40\,\mathrm{nm}$, with a thickness determined by the interplanar spacing of the graphene sheets, which is $0.335\,\mathrm{nm}$. Furthermore, the resulting structure was oriented in the simulation box such that the x and y axis directions corresponded to the zigzag and armchair edges, respectively.

After initial equilibration using an NVT ensemble at $300\,\mathrm{K}$ for $100\,\mathrm{ps}$, the mechanical properties of the CGMD graphene were investigated. By simulating a progressive box deformation along the x and y axes, an uniaxial strain was applied to the graphene along the armchair and zigzag directions, respectively. The internal stress components parallel to the deformation direction were measured, obtaining the stress–strain curve shown in Fig. 6.a. By measuring the slope in the elastic regime of the material, $\varepsilon \in [0.0, 0.05)$, indicated with the black dashed line in Fig. 6.a, we determined a Young's modulus of $916\,\mathrm{GPa}$ and a Poisson's ratio of 0.15 in the zigzag direction. Similarly, along the armchair direction, the slope of the curve in the elastic regime (gray dashed line in Fig. 6.a) yielded a Young's modulus of $845\,\mathrm{GPa}$ and a Poisson's ratio of 0.14. These results agree with literature values (900–1050 GPa and $0.14 - 0.19$) [71,72], confirming that the MARTINI force field adopted for graphene effectively describes the internal forces, even after the coarse-grained approximation.

Following the approach used for PLA, the thermal properties of pure graphene were investigated. The CGMD graphene underwent several NPT simulations with temperatures ranging from $300\,\mathrm{K}$ to $345\,\mathrm{K}$. By evaluating the average enthalpy from each simulation, the specific heat capacity (c_p) of the filler was computed. By linearly interpolating the data points in Fig. 6.b, we determined the specific heat capacity to be $430\,\mathrm{J/(kg\,K)}$. This value is approximately 40% lower than the experimental value of $700\,\mathrm{J/(kg\,K)}$ measured at room temperature [73]. As previously noted, such discrepancies are commonly observed in the literature [32] when using CGMD models, since the loss of vibrational DOF in CGMD simulations impact on the accurate description of kinetic energy and both inter- and intra-molecular interactions.

Since the filler aims to enhance both the mechanical strength and thermal conductivity of the final product, thereby improving the printing process and solidification, it is essential to investigate the thermal conductivity of pure graphene (Gr). However, working with relatively small systems and PBC introduces challenges. When phonons encounter a boundary, they can be reflected or transmitted, affecting their momentum and propagation, which in turn impacts the conductivity. To tackle this challenge, we utilize the ballistic-to-diffusive crossover formula [74]:

$$\frac{1}{\lambda(L)} = \frac{1}{\lambda_0}\left(1 + \frac{\mathcal{L}}{L}\right), \tag{6}$$

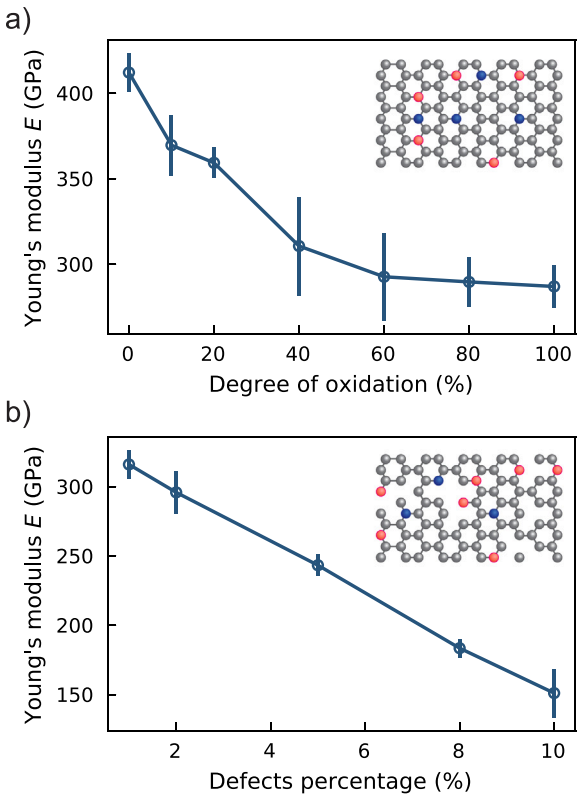

Fig. 7. Mechanical properties degradation for Graphene Oxide (GO) and reduced Graphene Oxide (rGO). (a) Young's modulus of GO at varying oxidation levels, with equal ratios of hydroxyl-oxidized (blue beads) and epoxide-oxidized (red beads) defects. (b) Young's modulus of coarse-grained rGO at different defect percentages, with a 4% oxidation level. Error bars show standard deviation from five replicas per system. (For interpretation of the references to color in this figure legend, the reader is referred to the web version of this article.)

where $\lambda(L)^{-1}$ is the reciprocal of the conductivity, also called thermal resistivity, L is the characteristic length of the sample, $\mathcal{L}$ represents the mean free path of phonons in graphene, and λ_0 denotes the thermal conductivity at infinite length. Thus, we constructed five additional CGMD Gr systems with simulation box lengths varying from 10 nm to 100 nm. The thermal conductivity was then computed using a similar NEMD method as used in the pure PLA study. The reciprocal of the resulting λ values was plotted against the inverse of the length, producing the graph shown in Fig. 6.c. By performing a linear fit on the data measured along the armchair and zigzag directions, we determined the intercept of the straight line, corresponding to a maximum resistivity of $0.0017\,\mathrm{m\,K/W}$ and $0.0015\,\mathrm{m\,K/W}$. This translates to a maximum conductivity of $588\,\mathrm{W/(m\,K)}$ and $667\,\mathrm{W/(m\,K)}$ for the armchair and zigzag directions, respectively. As expected, the simplification of the problem by reducing the degrees of freedom with CGMD beads resulted in an underestimation of the conductivity. Fully atomistic molecular dynamics studies in the literature report a thermal conductivity for graphene of $746\,\mathrm{W/(m\,K)}$ [74]. Similar to PLA, the reduced degrees of freedom in the mesoscale model lead to an underestimation of the kinetic energy and consequently its flux.

To enhance the composite morphology and functionality, incorporating Graphene Oxide (GO) and reduced Graphene Oxide (rGO) can significantly improve the nanocomposite properties. GO can markedly improve the dispersion of graphite flakes within the polymeric matrix, thereby optimizing the mechanical and thermal properties of the final product [75]. The functionalized surface of GO not only controls the dispersion or aggregation of the graphene flakes, providing additional material design flexibility, but also enhances the thermal and electrical properties of the polymer. This enhancement makes nanocomposites with GO and rGO suitable for a variety of advanced applications, including energy storage, stimuli-responsive materials, anticorrosion coatings, and separation processes [76]. To accurately develop our multiscale composite model, it is essential to recognize that pure and ideal graphene do not fully represent the material, as the addition of GO and rGO can significantly alter the mechanical properties of the nanocomposite. Therefore, we characterized the elastic modulus of the coarse-grained models for graphene oxide and reduced graphene oxide. The GO model included two new CGMD beads: one representing hydroxyl-oxidized groups (replacing 4 carbon atoms and the bonded hydroxyl group -OH) and another representing 2 carbon atoms and an epoxy group (C-O-C). Different grades of oxidation were modeled and subjected to tensile tests, considering an equal ratio (1:1) of hydroxyl-oxidized and epoxide-oxidized beads. From the stress–strain curves, the Young's modulus was computed by evaluating the slope in the elastic deformation region. A degradation of the modulus was observed with increasing degrees of oxidation, with values ranging from 412 GPa to 287 GPa, as shown in Fig. 7a. Fig. 7.b also presents the results of tensile stress tests for coarse-grained rGO with varying defect percentages. The rGO model was created by randomly deleting carbon beads from the GO model to simulate defects. The base model, a 4% degree of oxidation monolayer sheet of GO, was used to construct rGO sheets with different defect percentages. As expected, the Young's modulus decreased with increasing defect percentages, ranging from 316 GPa to 151 GPa.

However, it is important to note that the observed elastic modulus at 0% oxidation/defects, as depicted in Fig. 7, is lower than the modulus of pure graphene reported earlier in this study. This discrepancy arises due to the use of force field parameters from the GO model that account solely for carbon–carbon (C–C) interactions (type-I, refer to supplementary Table S7). Meng et al. [77], who developed the CG force field for GO, used these same parameters and observed similar results for pure graphene. This suggests that while the force field is effective for modeling GO at oxidation levels greater than 0%, it may not fully capture the properties of pure graphene. The lower elastic modulus at 0% oxidation highlights the impact of force field parameterization on the calculated properties, even for identical materials. This justify the necessity of using different force fields for Gr and GO/rGO to accurately capture the distinct mechanical behaviors of these fillers.

3.1.3. Polylactic acid nanocomposites (PLA/Gr, PLA/GO and PLA/rGO)

After the pure components investigation, a CGMD model of the nanocomposite was employed to comprehensively understand the impact of Gr, GO, and rGO inclusion on the thermo-physical properties of pure polylactic acid. Various concentrations of Gr, GO (60% oxidized), and rGO (4% oxidized with 10% defects) (namely: 0.5 wt%, 0.8 wt%, 1.0 wt%, 1.5 wt%, 2.0 wt%) were incorporated into the polylactic acid matrix. As an example, Fig. 8.d illustrates the equilibrated system of PLA reinforced with 2.0 wt% Gr.

Fig. 8.a provides a comparative analysis of the relative Young's moduli for the PLA/Gr, PLA/GO, and PLA/rGO nanocomposites. The inclusion of Gr, GO, and rGO significantly enhances the Young's modulus of pure PLA. Specifically, the Young's modulus of PLA/Gr nanocomposites increases from 4.60% (0.5 wt%) to 11.54% (2.0 wt%). Due to the finite size of the simulation box and the distribution of fillers, variations in elasticity along the x, y, and z directions are observed, even though the property is isotropic. Therefore, values are averaged across directions, resulting in mean value and error as shown in Fig. 8.a. In PLA/GO nanocomposites, the Young's modulus rises from 1.69% (0.5 wt%) to 8.18% (2.0 wt%), while PLA/rGO nanocomposites exhibit an increase from 0.6% (0.5 wt%) to 7.7% (2.0 wt%). Among these, PLA/Gr nanocomposites demonstrate superior mechanical properties compared to PLA/GO and PLA/rGO nanocomposites, in line with the mechanical performance of fillers alone.

The impact of Gr, GO, and rGO on the thermal conductivity of PLA was investigated to understand their potential enhancements. The trends are illustrated in Fig. 8.b, which depicts the relative thermal

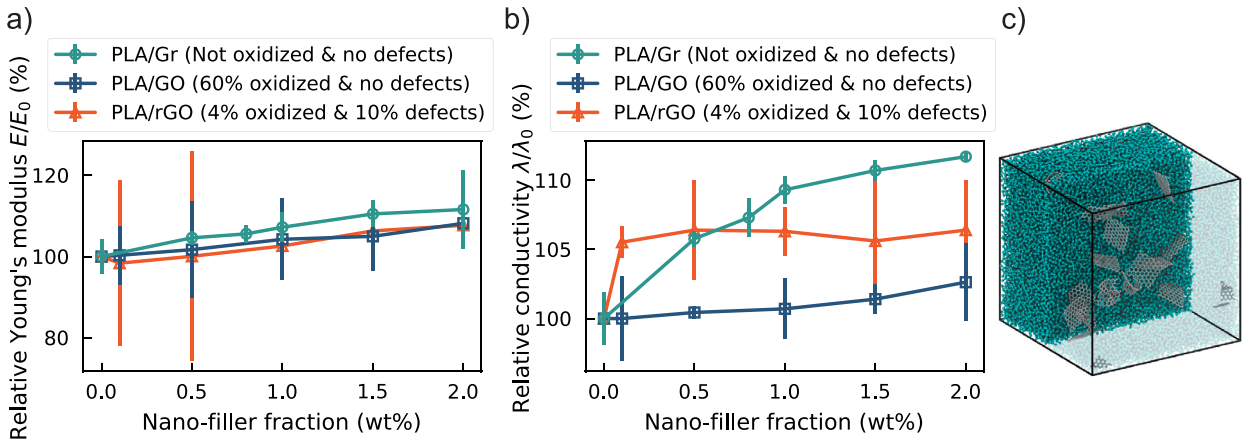

Fig. 8. Influence of nanofillers on coarse-grained nanocomposite models for Young's modulus (E) (a) and thermal conductivity (λ) (b), normalized to pure PLA values ($E_0 = 1.65\,\text{GPa}$, $\lambda_0 = 0.113\,\text{W/(m K)}$). Graphs show effects of graphene (Gr) in green, 60% oxidized graphene (GO) in blue, and 10% reduced/4% oxidized graphene (rGO) on PLA in orange. (c) Rendering of CGMD PLA/Gr (2.0 wt%) nanocomposite. (For interpretation of the references to color in this figure legend, the reader is referred to the web version of this article.)

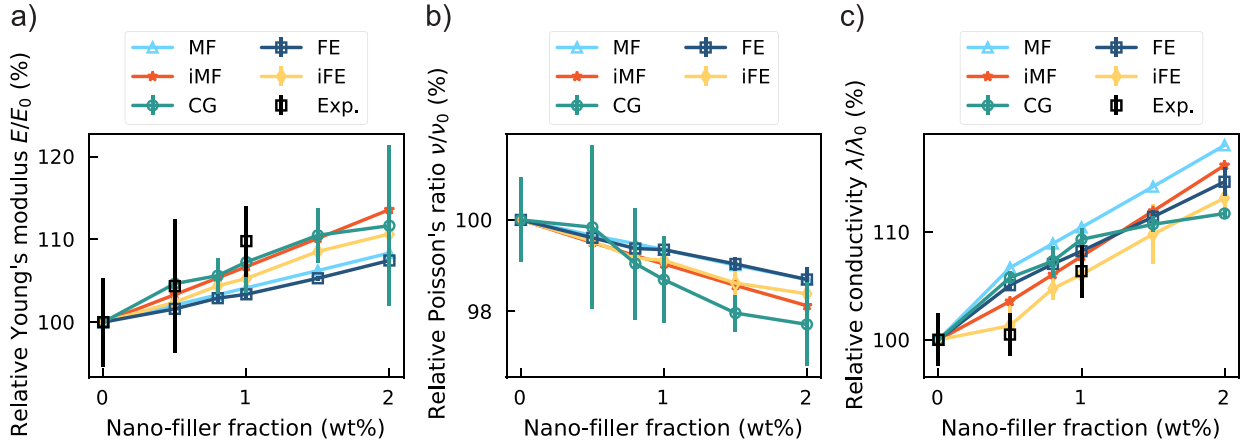

Fig. 9. Influence of the nano-filler on the Young's modulus (E) (a), Poisson's ratio (ν) (b), and thermal conductivity (λ) (c) of the composite, predicted using multiscale models. Five techniques are represented: mean field (MF, cyan), interphase mean field (iMF, orange), coarse-grained model (CGMD, green), finite elements (FE, blue), and interphase finite elements (iFE, yellow). Experimental values for PLA/GNPs nanocomposites are shown as black squares. Data are normalized to bulk PLA values (0.0 wt%). (For interpretation of the references to color in this figure legend, the reader is referred to the web version of this article.)

conductivity of the composite material at room temperature as a function of the weight percentage of Gr, GO, and rGO nanofillers. As with Young's modulus, we assume isotropic conductivities, averaging values across the x, y, and z directions to obtain a mean and associated error, as shown in Fig. 8.b. Pure PLA exhibits a low thermal conductivity of $0.112\,\text{W/(m K)}$. Our results demonstrate a slight increase in thermal conductivity with the addition of nanofillers. For PLA/Gr nanocomposites, the maximum observed thermal conductivity was $0.125\,\text{W/(m K)}$ at 2.0 wt%, representing an improvement of 11.6%. In contrast, the PLA/GO nanocomposites showed thermal conductivity values very close to that of pure PLA. Similarly, PLA/rGO nanocomposites exhibited trends akin to PLA/Gr nanocomposites, with an average maximum thermal conductivity of $0.121\,\text{W/(m K)}$ at 2.0 wt%, matching the maximum value for PLA/Gr composites. Thus, our findings indicate that, up to 2.0 wt%, graphene fillers enhance the thermal conductivity of the PLA matrix by approximately 10%, consistent with the observed improvements in mechanical properties. However, the absolute enhancement in conductivity may seem lower than intuitively expected, given the order of magnitude difference between the conductivities of PLA and graphene. This is due to the significant interfacial thermal resistance (Kapitza resistance), which, for fillers with such a high aspect ratio and limited thermal conductivity due to their size, has a non-negligible effect.

To enhance the robustness of our nanocomposite modeling, we compared it with respect to Mean Field and Finite Element models. This integration aimed to evaluate these methods as potential alternatives and assess their contribution to the overall comprehensiveness of the study. While continuum approaches like MF and FE offer valuable insights, they inherently lack the ability to accurately capture filler–matrix interactions and the effects of interface functionalizations. This shortcoming is mitigated by mesoscopic simulations, which provide a molecular-level understanding of these interactions. To ensure a comprehensive comparison, we juxtaposed the predictions from our CGMD model with those from continuum approaches. Following the linked multiscale protocol depicted in Fig. 1, input parameters for the constituents were derived from coarse-grained simulation results. For PLA, the parameters included a density of $\rho^{PLA} = 1.188\,\text{g/cm}^3$, an elastic constant of $E^{PLA} = 1.6\,\text{GPa}$, a Poisson's ratio of $\nu^{PLA} = 0.38$, a specific heat capacity of $c_p^{PLA} = 446.5\,\text{J/(kg K)}$, and a thermal conductivity of $\lambda^{PLA} = 0.112\,\text{W/(m K)}$. For graphene, the parameters were a density of $\rho^{Gr} = 1.402\,\text{g/cm}^3$, an elastic constant of $E^{Gr} = 916\,\text{GPa}$, a Poisson's ratio of $\nu^{Gr} = 0.15$, a specific heat capacity of $c_p^{Gr} = 430\,\text{J/(kg K)}$, and a thermal conductivity of $\lambda^{Gr} = 628\,\text{W/(m K)}$, which is an average value of the two directions previously computed. Subsequently, the Representative Volume Element (RVE) model was generated. We selected various mass fractions (0.5, 0.8, 1.0, 1.5, 2.0 wt%) and introduced a corresponding number of graphene inclusions, dispersed randomly within the PLA matrix, mirroring the setup of our CGMD models. This approach allowed us to rigorously evaluate the multiscale modeling

technique, providing a detailed comparison between mesoscopic and continuum methods. The results obtained from the FE and MF models were compared with those from the CGMD simulations in Fig. 9. For all properties and each model, we assumed isotropic materials, measuring each property along the three orthogonal directions and averaging the results, with error bars representing deviations shown in Fig. 9. In the CGMD simulations, the Young's modulus increased from 4.60% (0.5 wt%) to 11.54% (2.0 wt%) compared with bulk PLA, whereas the FE and MF models showed an increase from 1.60% (0.5 wt%) to 7.44% (2.0 wt%) as shown in Fig. 9.a. This indicates that both FE and MF models underestimate the Young's modulus enhancement provided by graphene inclusions. In contrast, the CGMD model delivers more accurate results by modeling the filler–matrix interaction with molecular precision. Fig. 9.b illustrates the Poisson's ratio of PLA/Gr composites as predicted by mesoscopic and continuum models. The CGMD, FE, and MF models all predict a progressive reduction in Poisson's ratio with increasing graphene concentrations. However, the CGMD simulation predicts a more significant reduction compared to both FE and MF models. To address the limitations of matrix–filler interactions in continuum approaches, Ji et al. [78] proposed an interphase micromechanical model based on the Takayanagi homogenization technique, incorporating interfacial contributions. Therefore, an interphase was similarly introduced as a coating on the filler in the finite element and mean field models, characterized by a thickness of $0.5\,\mathrm{nm}$ and an elastic modulus of $3\,\mathrm{GPa}$. The interphase thickness of $0.5\,\mathrm{nm}$ was determined by analyzing the radial distribution function (RDF) of PLA molecules around the fillers from the CGMD simulations, which helped identify the affected region. The elastic modulus of $3\,\mathrm{GPa}$ was derived from CGMD simulations and used as a reference to accurately parameterize the mechanical properties of the interphase in our models [32]. This approach reflects the significantly enhanced elastic modulus of the interphase, similar to the findings of other studies [79–82] which have shown that the polymeric region adjacent to the filler exhibits increased mechanical properties compared to the bulk matrix. Incorporating this interphase led to the development of the interphase finite element model (iFE) and the interphase mean field model (iMF). Fig. 9 illustrates that the results from the iMF and iFE models, represented by the cyan and yellow lines, demonstrate strong agreement with the coarse-grained simulation results.

Fig. 9.c presents a comparison of the thermal conductivity of PLA/Gr composites as predicted by mesoscopic and continuum approaches. The thermal conductivity of PLA composite material increases with the weight percentage of graphene fillers in all cases. However, CGMD predictions show a lower enhancement due to the consideration of thermal boundary resistance at the filler–filler and filler–matrix interfaces. To address this issue in continuum approaches, similar to the methodology for mechanical properties, a Kapitza resistance was introduced at the interphase between the polymer and graphene, with a value of $3.7\times10^{-9}\,\mathrm{K\,m^2/W}$ [83]. This adjustment led to a thermal conductivity of the interface of approximately $0.135\,\mathrm{W/(m\,K)}$, which aligns closely with the CGMD thermal conductivity of pure PLA. By incorporating thermal boundary resistance at the filler–matrix interface, the continuum model results achieved good agreement with the CGMD results.

In practical applications, single-layer graphene is not commercially available; it is typically obtained as graphene nanoplatelets (GNPs), composed of stacked graphene sheets. The properties of polymer composites are influenced by factors such as filler dispersibility, interface adhesion, and filler morphology [84,85]. Generally, the elastic modulus and thermal conductivity of nanocomposites increase with the aspect ratio of the platelets [86]. However, larger GNPs often suffer from inadequate dispersion, leading to the formation of massive agglomerates. This phenomenon is mitigated at the low concentrations studied in this work. Conversely, increasing the aspect ratio of GNPs can induce wrinkling, negatively affecting the effective ratio of the fillers and diminishing their overall contribution to mechanical and thermal properties. In this study, the aspect ratio of GNPs used for experimental characterization ranged from 500 to 1000, deviating significantly from the actual aspect ratio of the fillers incorporated into the composites.

To provide context for our modeling approach, previous studies have highlighted the importance of considering the effective aspect ratio of GNPs. Kalaitzidou et al. [87] found that the elastic modulus of xGnP-15/PP composites was overestimated using the Halpin–Tsai and Tandon–Weng models due to the theoretical aspect ratio of ~1500, whereas the effective aspect ratio during processing was at least an order of magnitude smaller [87]. Similarly, Jun et al. [88] demonstrated that the predicted modulus of PP/GNP composites using the Halpin–Tsai equation was higher than experimental values, which was corrected by using a measured aspect ratio of ~50 instead of the theoretical value. Innes et al. [89] also noted that the effective aspect ratio contributing to the enhancement of the elastic modulus was significantly smaller than the manufacturer's anticipated value.

These findings underscore the necessity of appropriately adjusting theoretical parameters to accurately predict the properties of GNPs within composites. In this study, we used an effective aspect ratio of 50, measured after composite processing, instead of the nominal aspect ratio. This approach ensures a more accurate prediction of the elastic modulus and thermal conductivity, providing a realistic representation of the material behavior, as demonstrated by Muhammad et al. [32].

The interphase mean field model was utilized to evaluate the Young's modulus and thermal conductivity of PLA nanocomposites reinforced with graphene nanoplatelets (PLA/GNPs), as tested in the experiments. The model input parameters were aligned with experimental data: polylactic acid had a density of $1.24\,\mathrm{g/cm^3}$, a Young's modulus of $1.84\,\mathrm{GPa}$, a Poisson's ratio of 0.36, and a thermal conductivity of $0.204\,\mathrm{W/(m\,K)}$. For graphene, the properties included a density of $2.2\,\mathrm{g/cm^3}$, an effective aspect ratio of 50, a Young's modulus of $1030\,\mathrm{GPa}$, a Poisson's ratio of 0.19, and a thermal conductivity of $3000\,\mathrm{W/(m\,K)}$. The interphase properties were derived by fitting the CGMD results.

Overall, the Mori–Tanaka MF model, incorporating an interphase (iMF) and an effective aspect ratio, provides predictions for the elastic modulus and thermal conductivity of PLA/GNPs that align well with experimental results. The maximum deviations are 1.9% for E and 2.3% for λ within the $[0, 1]$ wt% filler interval, as shown in Fig. 10. Following the workflow represented in Fig. 1, the thermal and elastic properties reported in this section were used as input for the models developed to predict the homogenized properties of 3D printing materials. The results of these predictions are presented in the next section.

3.2. Properties prediction for 3D printed PLA composites

The final specimens resulting from printing the nanocomposite filament were thoroughly investigated. The manufacturing process frequently results in the formation of void channels between filaments, leading to the formation of an anisotropic material. To examine the internal structure of the printed samples (Fig. 4), cross-sections were prepared and analyzed using optical microscopy, which revealed a non-uniform distribution of defects throughout the material. Quantitative analysis indicated a global porosity of approximately 0.87%, with significant variations observed across different regions of the samples. The observed defects were predominantly triangular in shape, with occasional rhomboidal formations also identified. Detailed measurements of defect geometry and spacing were conducted, following the methodology outlined in Section 2.2 of the Methods.

Consequently, to comprehensively assess the impact of these defects, five different possible defect sizes and shapes were analyzed, as illustrated in Fig. 12.a. Mechanical and thermal properties were subsequently measured for the nanocomposite systems (i.e., PLA/Gr, PLA/GO, and PLA/rGO), as well as for the printed structures characterized by an average triangular (Triangle M) pattern, illustrated in

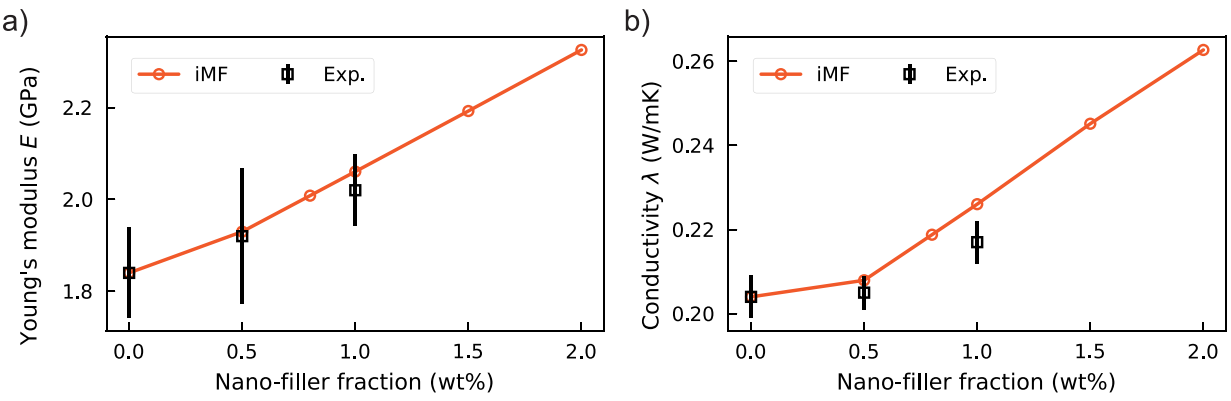

Fig. 10. Comparison of interphase mean field model (iMF) predictions and experimental data (Exp.) for Young's modulus (a) and thermal conductivity (b) of nanocomposites with graphene nanoplatelets (PLA/GNPs) at different weight percentages of nanofillers. The lines representing model predictions serve as guides for the eye to illustrate trends also over the filler wt% measured experimentally.

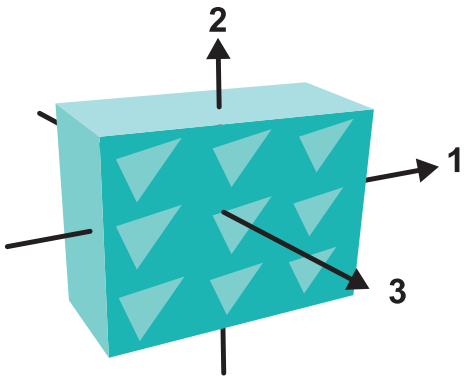

Fig. 11. Reference frame for the experimental specimens and FE model used to investigate the anisotropic properties resulting from the manufacturing process.

Table 3
Thermal conductivity of the bulk materials obtained from finite element analysis compared with the directional thermal conductivities of 3D printed structures, using the average size porosity defects specified as Triangle M (Fig. 12.a).

Material system	λ (W/(m K))	λ_{11} (W/(m K))	λ_{22} (W/(m K))	λ_{33} (W/(m K))
PLA	0.112	0.1047	0.1027	0.1096
PLA/Gr 2%	0.121	0.1102	0.1081	0.1154
PLA/rG0 2%	0.125	0.1130	0.1108	0.1182

Fig. 12.a.i. Additionally, these properties were evaluated in different directions, as illustrated in Fig. 11, to measure the anisotropy of each property.

For the thermal properties, the directional conductivities estimated by the FE analysis for the different material systems are reported in Table 3. In this context, λ_{33} represents the conductivity in the printing filament direction, while λ_{11} and λ_{22} denote the conductivities in the transversal directions, as indicated by the axes in Fig. 11. The results indicate that the printing process induces anisotropy in thermal conductivity due to the distribution and shape of defects with variations up to 6.7% between maximum and minimum conductivities in different directions. This result is in line with thermal conductivity variations experimentally characterized in various works for FDM/FFF 3D printing polymers [90,91]. Notably, even the two transversal directions exhibit slight differences in conductivity attributable to the defect shapes. The thermal conductivities used to inform the FE models in this study were derived from the CGMD models discussed previously. These values were used as bulk properties for defining the material constituents.

The PLA was analyzed in its pure form, doped with 2 wt% of graphene, and doped with 2 wt% of reduced graphene oxide, which represents the maximum concentration within the studied range aimed at achieving the highest properties improvement. It was observed that the ratio between each directional conductivity and the bulk material conductivity remains consistent across all materials, being solely dependent on the material structure.

Similarly, the directional thermal conductivities of the five structures depicted in Fig. 12.a were calculated for the base material system, neat PLA. It is important to note that the porosity of each structure is influenced by the size and number of defects, regardless of the defect shape. The resulting conductivities are presented in Fig. 12.b (for detailed numerical values, see Table S1 in the supplementary material). It can be observed that as the porosity increases, anisotropy becomes more pronounced, resulting in a greater difference between the conductivity in the filament direction and the transversal values. Additionally, the dependence of the conductivity on porosity is clearly linear within the studied range.

Regarding the mechanical properties, the results obtained from the CGMD models for pure and doped PLA were used to define the constituent behaviors. PLA, PLA/Gr, and PLA/rGO, each with 2 wt%, were analyzed using the average triangular defect size (structure Triangle M sketched in Fig. 12.a.i) to evaluate the effect of voids. The mechanical properties of the 3D printed material, in terms of elastic constants, are included in Table 4. It was observed that the values of the elastic moduli and shear moduli are proportional to the elastic modulus of the bulk material in each case, indicating that this relationship is solely dependent on the material structure. Additionally, the predicted Poisson's ratios remain constant across all material systems, as they are considered to be the same in each case. The anisotropy observed in the elastic moduli is greater in relative terms (approx. 12% variation between maximum and minimum Young's moduli in different directions). The differences are in line with results reported in other studies, as in the work of Song et al. [92], where relative variations up to 4.7% were observed in the tensile elastic modulus of 3D printed PLA in different directions with a porosity close to 1% (lower than the one of average triangle – Fig. 12.a.i). In the work of Chacón et al. [8], differences around 16% in different directions are reported for the same property, depending on the PLA processing conditions.

Similarly, the mechanical behavior of the structures with bulk PLA material properties is analyzed in terms of elastic constants. The predicted values as a function of the structure porosity are represented in Fig. 12.c, .d, and .e. The corresponding numerical values can be found in Table S2 of the supplementary material. It is observed that all parameters are influenced by the void structure. Interestingly, for similar porosity values, some parameters exhibit higher variability depending on the structure. For example, cases Triangle M (i), Triangle L (ii), and Alternated Triangle (iv) have almost the same porosity, but parameters such as E_{22} and ν_{23} show significant differences, while

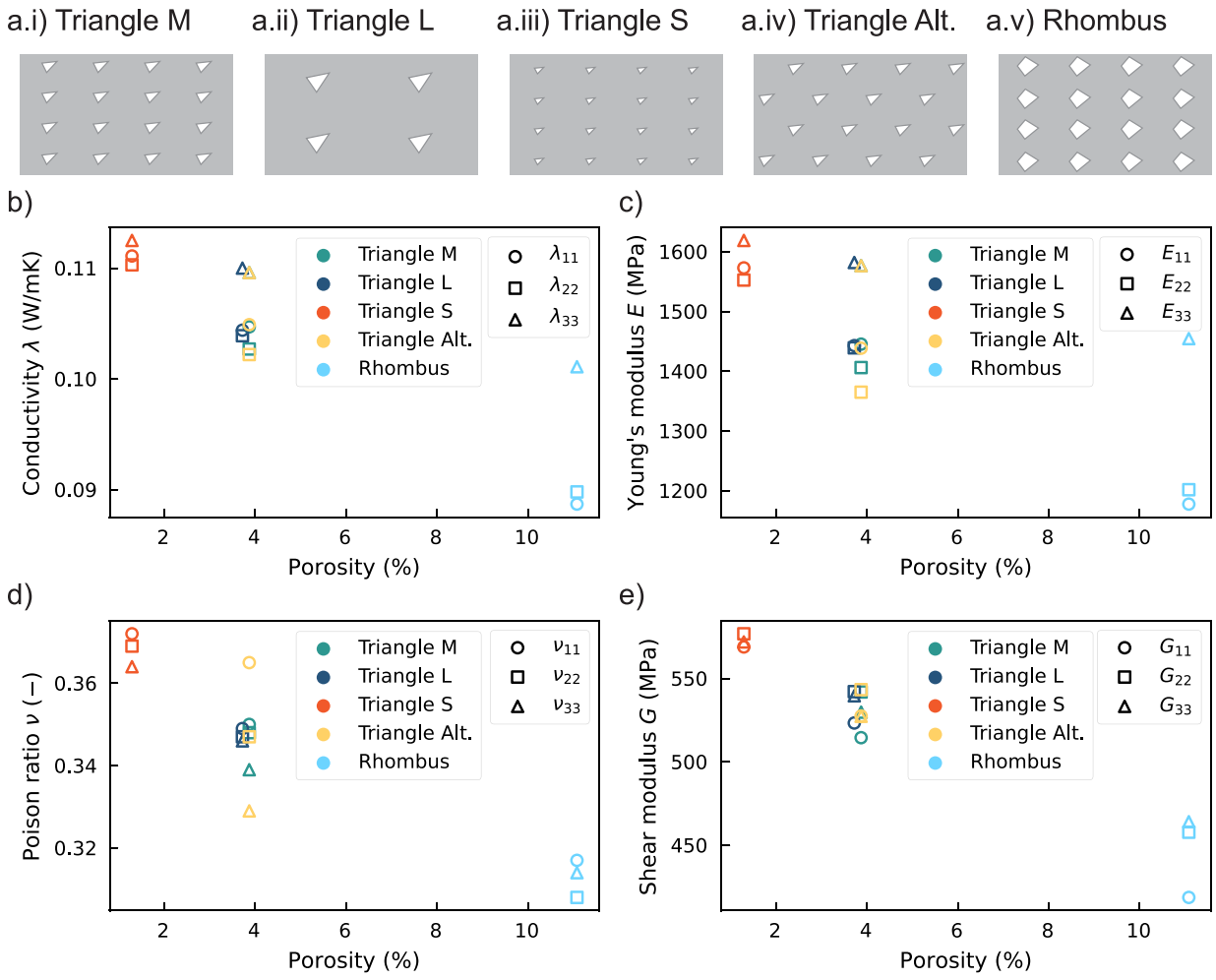

Fig. 12. Influence of modeled porosity on conductivity (b), Young's modulus (c), Poisson's ratio (d), and shear modulus (e). Various defect shapes, as sketched in (a), are represented using the color code indicated in the legend. Different marker shapes are used to visualize the orientations where the properties were evaluated. (For interpretation of the references to color in this figure legend, the reader is referred to the web version of this article.)

Table 4
Mechanical properties derived from finite element analysis of pure PLA and carbon-based nanocomposite systems, incorporating the average defect size structure (Triangle M, as shown in Fig. 12.a). Young's modulus (E) was evaluated along principal strain directions (1, 2, and 3), while Poisson's ratio (ν) and shear modulus (G) were assessed along corresponding shear planes (1 2, 1 3, and 2 3).

Material system	E_{11} (MPa)	E_{22} (MPa)	E_{33} (MPa)	ν_{12} (–)	ν_{13} (–)	ν_{23} (–)	G_{12} (MPa)	G_{13} (MPa)	G_{23} (MPa)
PLA	1445.3	1406.1	1576.6	0.35	0.348	0.339	514.5	541.9	529.8
PLA/Gr 2%	1621.5	1577.6	1768.9	0.35	0.348	0.339	577.2	608.1	594.4
PLA/rG0 2%	1563.8	1521.4	1705.9	0.35	0.348	0.339	556.7	586.4	573.3

parameters like E_{11} and ν_{12} have very similar values. This highlights that both porosity and the distribution/shape of defects significantly affect the material behavior.

Overall, these findings underscore the importance of considering both porosity and defect distribution/shape when predicting the mechanical properties of 3D printed PLA nanocomposites. A multiscale model, such as the one proposed, can serve as a valuable tool in material design. In relation with the graphene particles addition, as expected, the improvements obtained in the whole set of elastic constants is proportional to the enhancement introduced in the filament material properties definition. These trend agrees with previous works in the literature, as in the work of Cataldi et al. [93] or in the review of Silva et al. [94].

4. Conclusions

In this work, we presented a comprehensive multiscale approach to accurately determine the thermal and mechanical properties of 3D printed nanocomposite filaments, bridging scales from molecular interactions to full component performance.

In detail, we performed CGMD simulations that successfully reproduced the thermophysical properties of PLA, Gr, GO and rGO. These CGMD models were then coupled to reproduce *in silico* samples of PLA/Gr, PLA/GO, and PLA/rGO nanocomposites. Our study demonstrated that even low concentrations of fillers significantly impact the properties of PLA/Gr, PLA/GO, and PLA/rGO nanocomposites. Young's modulus and thermal conductivity are enhanced with increasing percentage of Gr, GO as well rGO. However, the mechanical and thermal properties of PLA/Gr nanocomposites were found to be superior to

those of PLA/GO and PLA/rGO nanocomposites. For the multiscale nature of the problem, we then upscaled CGMD model of PLA/Gr to continuum model using results obtained at the CGMD level in MF and FE analyses. The CGMD predictions were verified by the MF model with interphase, which demonstrated superior predictive capability compared to traditional continuum approaches due to detailed modeling of the filler–matrix interactions. The MF model with interphase was validated against experimental results, showing excellent agreement.

Furthermore, the homogenized thermal conductivities and elastic properties of a 3D printed material made of the PLA-based nanocomposites have been evaluated. Through optical microscopy analysis, we characterized the internal structure of printed samples, identifying shape and dimension of microstructural defects resulting from the printing process. These observations informed FE simulations, which were used to model various internal morphologies and integrate the thermal and elastic properties from the CGMD models. Several combinations of structure and material composition were analyzed using this bottom-up informed continuum model, enabling the observation of their effects:

- For a given material structure, the ratios between the homogenized and the bulk material properties depend only on the structure and not on the bulk material properties.
- The porosity of the printed material is a crucial parameter when modifying the material structure without changing the material properties.
- For a fixed porosity, the effect of the defect's shape is smaller in the printing direction than in the transversal ones, because in the printing direction the effective area of the section remains constant for a given porosity independently of the defect's shape.

The proposed multiscale approach not only enhances predictive accuracy, but also serves as a versatile tool for advancing nanocomposite material design. By capturing the effects of filler–matrix interactions, structural defects, and porosity, this model can support the optimization of 3D [5,15] and 4D printed [24] functionalized devices, paving the way for the development of more efficient and effective nanocomposite technologies in various mechanical applications. Regarding broader implications of this work, CGMD models are limited in predicting electromagnetic properties due to their coarse-grained nature, which lacks the electronic detail required for accurate conductivity predictions. For conductive materials like graphene, electronic properties are better captured by quantum mechanical or ab initio simulations. Future studies could incorporate such electronic models for electrical property evaluation, extending the applicability beyond mechanical reinforcement (e.g., sensing [95]).

CRediT authorship contribution statement

Atta Muhammad: Writing – original draft, Software, Methodology, Investigation, Formal analysis. **Clara Valero:** Writing – original draft, Software, Methodology, Investigation, Formal analysis. **Paolo De Angelis:** Writing – original draft, Visualization, Validation, Formal analysis, Data curation. **Nikolaos Koutroumanis:** Writing – review & editing, Investigation, Formal analysis. **Dionisis Semitekolos:** Writing – review & editing, Methodology, Investigation, Formal analysis. **Bárbara Jiménez:** Methodology, Investigation. **Rubén Rivera:** Methodology, Investigation, Formal analysis. **Carlos Sáenz Ezquerro:** Writing – original draft, Software, Investigation, Formal analysis. **Rajat Srivastava:** Writing – review & editing, Methodology. **Panagiotis-Nektarios Pappas:** Writing – review & editing, Resources. **Costas Galiotis:** Writing – review & editing, Resources. **Costas A. Charitidis:** Writing – review & editing, Supervision, Resources, Funding acquisition. **Eliodoro Chiavazzo:** Writing – review & editing, Supervision. **Pietro Asinari:** Writing – review & editing, Supervision, Funding acquisition. **Manuel Laspalas:** Writing – review & editing, Methodology, Investigation, Formal analysis. **Agustín Chiminelli:** Writing – review & editing, Supervision, Project administration, Funding acquisition, Conceptualization. **Matteo Fasano:** Writing – review & editing, Supervision, Project administration, Conceptualization.

Code availability

All molecular dynamics (MD) simulations in this study were performed using the open-source LAMMPS (Large-scale Atomic/Molecular Massively Parallel Simulator) software package [96].

Declaration of competing interest

The authors declare that they have no known competing financial interests or personal relationships that could have appeared to influence the work reported in this paper.

Acknowledgments

The project leading to this application was funded by the European Union's Horizon 2020 research and innovation programme under grant agreement No. 760779 (SMARTFAN project) and through COST Action CA19118 (EsSENce), which is supported by the European Cooperation in Science and Technology (COST). A.M. received a research scholarship from the Higher Education Commission (HEC) and the Government of Pakistan under the "HRD Initiative-MS leading to Ph.D. program for faculty development for UESTPs/UETs, Phase-I (Batch-V)" for studies at Politecnico di Torino, Italy.

Computational resources were provided by HPC@POLITO, a project of Academic Computing within the Department of Control and Computer Engineering at Politecnico di Torino (http://www.hpc.polito.it).

The authors also thank doctor Vittorio Morandi and his team from IMM-CNR Bologna, Italy (https://www.imm.cnr.it) for conducting the SEM analysis.

Appendix A. Supplementary data

Supplementary material related to this article can be found online at https://doi.org/10.1016/j.compositesb.2025.112354.

Data availability

In accordance with FAIR principles to ensure full reproducibility of this work, all simulation input files, raw experimental data, and related pre-processing and post-processing scripts are publicly available. These materials can be accessed through the GitHub repository at https://github.com/paolodeangelis/CGMD_PLA-Gr and the Zenodo repository at https://doi.org/10.5281/zenodo.14056590.

References

[1] Gibson I, Rosen DW, Stucker B. Additive manufacturing technologies: 3D printing, rapid prototyping and direct digital manufacturing. 2nd ed.. New York London: Springer; 2015.

[2] Ngo TD, Kashani A, Imbalzano G, Nguyen KT, Hui D. Additive manufacturing (3D printing): A review of materials, methods, applications and challenges. Compos Part B: Eng 2018;143:172–96. http://dx.doi.org/10.1016/j.compositesb.2018.02.012, URL: https://linkinghub.elsevier.com/retrieve/pii/S1359836817342944.

[3] Morciano M, Alberghini M, Fasano M, Almiento M, Calignano F, Manfredi D, Asinari P, Chiavazzo E. 3D printed lattice metal structures for enhanced heat transfer in latent heat storage systems. J Energy Storage 2023;65:107350. http://dx.doi.org/10.1016/j.est.2023.107350, URL: https://linkinghub.elsevier.com/retrieve/pii/S2352152X23007478.

[4] Brenken B, Barocio E, Favaloro A, Kunc V, Pipes RB. Fused filament fabrication of fiber-reinforced polymers: A review. Addit Manuf 2018;21:1–16. http://dx.doi.org/10.1016/j.addma.2018.01.002, URL: https://linkinghub.elsevier.com/retrieve/pii/S2214860417304475.

[5] Chen J, Su R, Zhang X, Li Y, He R. 3D printed leaf-vein-like Al_2O_3 /EP biohybrid structures with enhanced thermal conductivity. ACS Appl Mater Interfaces 2024;acsami.4c14564. http://dx.doi.org/10.1021/acsami.4c14564, URL: https://pubs.acs.org/doi/10.1021/acsami.4c14564.

[6] Coppola B, Cappetti N, Di Maio L, Scarfato P, Incarnato L. 3D printing of PLA/clay nanocomposites: Influence of printing temperature on printed samples properties. Materials 2018;11:1947. http://dx.doi.org/10.3390/ma11101947, URL: http://www.mdpi.com/1996-1944/11/10/1947.

[7] Yao T, Deng Z, Zhang K, Li S. A method to predict the ultimate tensile strength of 3D printing polylactic acid (PLA) materials with different printing orientations. Compos Part B: Eng 2019;163:393–402. http://dx.doi.org/10.1016/j.compositesb.2019.01.025, URL: https://linkinghub.elsevier.com/retrieve/pii/S1359836818323035.

[8] Chacón J, Caminero M, García-Plaza E, Núñez P. Additive manufacturing of PLA structures using fused deposition modeling: Effect of process parameters on mechanical properties and their optimal selection. Mater Des 2017;124:143–57. http://dx.doi.org/10.1016/j.matdes.2017.03.065, URL: https://linkinghub.elsevier.com/retrieve/pii/S0264127517303143.

[9] Tessarin A, Zaccariotto M, Galvanetto U, Stocchi D. A multiscale numerical homogenization-based method for the prediction of elastic properties of components produced with the fused deposition modeling process. Results Eng 2022;14:100409. http://dx.doi.org/10.1016/j.rineng.2022.100409, URL: https://linkinghub.elsevier.com/retrieve/pii/S2590123022000792.

[10] Tao Y, Kong F, Li Z, Zhang J, Zhao X, Yin Q, Xing D, Li P. A review on voids of 3D printed parts by fused filament fabrication. J Mater Res Technol 2021;15:4860–79. http://dx.doi.org/10.1016/j.jmrt.2021.10.108, URL: https://linkinghub.elsevier.com/retrieve/pii/S2238785421012448.

[11] Rahmatabadi D, Soltanmohammadi K, Aberoumand M, Soleyman E, Ghasemi I, Baniassadi M, Abrinia K, Bodaghi M, Baghani M. 4D printing of porous PLA-TPU structures: effect of applied deformation, loading mode and infill pattern on the shape memory performance. Phys Scr 2024;99:025013. http://dx.doi.org/10.1088/1402-4896/ad1957, URL: https://iopscience.iop.org/article/10.1088/1402-4896/ad1957.

[12] Garzon-Hernandez S, Garcia-Gonzalez D, Jérusalem A, Arias A. Design of FDM 3D printed polymers: An experimental-modeling methodology for the prediction of mechanical properties. Mater Des 2020;188:108414. http://dx.doi.org/10.1016/j.matdes.2019.108414, URL: https://linkinghub.elsevier.com/retrieve/pii/S0264127519308524.

[13] Monaldo E, Marfia S. Computational homogenization of 3D printed materials by a reduced order model. Int J Mech Sci 2021;197:106332. http://dx.doi.org/10.1016/j.ijmecsci.2021.106332, URL: https://linkinghub.elsevier.com/retrieve/pii/S0020740321000679.

[14] Tronvoll SA, Welo T, Elverum CW. The effects of voids on structural properties of fused deposition modelled parts: a probabilistic approach. Int J Adv Manuf Technol 2018;97:3607–18. http://dx.doi.org/10.1007/s00170-018-2148-x, URL: http://link.springer.com/10.1007/s00170-018-2148-x.

[15] Ma T, Zhang Y, Ruan K, Guo H, He M, Shi X, Guo Y, Kong J, Gu J. InfoMat 2024;6:e12568. http://dx.doi.org/10.1002/inf2.12568, URL: https://onlinelibrary.wiley.com/doi/10.1002/inf2.12568.

[16] Li H, Liu B, Ge L, Chen Y, Zheng H, Fang D. Mechanical performances of continuous carbon fiber reinforced PLA composites printed in vacuum. Compos Part B: Eng 2021;225:109277. http://dx.doi.org/10.1016/j.compositesb.2021.109277, URL: https://linkinghub.elsevier.com/retrieve/pii/S1359836821006533.

[17] Behera K, Chen J-F, Yang J-M, Chang Y-H, Chiu F-C. Evident improvement in burning anti-dripping performance, ductility and electrical conductivity of PLA/PVDF/PMMA ternary blend-based nanocomposites with additions of carbon nanotubes and organoclay. Compos Part B: Eng 2023;248:110371. http://dx.doi.org/10.1016/j.compositesb.2022.110371, URL: https://linkinghub.elsevier.com/retrieve/pii/S1359836822007442.

[18] Ensinger. TECAFIL PEEK VX CF30 black 1 75 mm - 500 g. 2024, URL: https://filaments.ensingerplastics.com/products/carbon-fiber-peek-filament-tecafil-peek-vx-cf30-black-1-75-mm-500g. (Accessed 12 January 2024).

[19] Filament2print. Graphene filaments for 3D printing. 2024, URL: https://filament2print.com/gb/14_graphene-3d-labs. (Accessed 12 January 2024).

[20] Arunkumar N, Sathishkumar N, Sanmugapriya S, Selvam R. Study on PLA and PA thermoplastic polymers reinforced with carbon additives by 3D printing process. Mater Today: Proc 2021;46:8871–9. http://dx.doi.org/10.1016/j.matpr.2021.05.041, URL: https://linkinghub.elsevier.com/retrieve/pii/S2214785321036178.

[21] Caminero M, Chacón J, García-Plaza E, Núñez P, Reverte J, Becar J. Additive manufacturing of PLA-based composites using fused filament fabrication: Effect of graphene nanoplatelet reinforcement on mechanical properties, dimensional accuracy and texture. Polymers 2019;11:799. http://dx.doi.org/10.3390/polym11050799, URL: https://www.mdpi.com/2073-4360/11/5/799.

[22] Aumnate C, Pongwisuthiruchte A, Pattananuwat P, Potiyaraj P. Fabrication of ABS/graphene oxide composite filament for fused filament fabrication (FFF) 3D printing. Adv Mater Sci Eng 2018;2018:1–9. http://dx.doi.org/10.1155/2018/2830437, URL: https://www.hindawi.com/journals/amse/2018/2830437/.

[23] Masarra N-A, Batistella M, Quantin J-C, Regazzi A, Pucci MF, El Hage R, Lopez-Cuesta J-M. Fabrication of PLA/PCL/graphene nanoplatelet (GNP) electrically conductive circuit using the fused filament fabrication (FFF) 3D printing technique. Materials 2022;15:762. http://dx.doi.org/10.3390/ma15030762, URL: https://www.mdpi.com/1996-1944/15/3/762.

[24] Bodaghi M, Wang L, Zhang F, Liu Y, Leng J, Xing R, Dickey MD, Vanaei S, Elahinia M, Hoa SV, Zhang D, Winands K, Gries T, Zaman S, Soleimanzadeh H, Barši Palmić T, Slavič J, Tadesse Y, Ji Q, Zhao C, Feng L, Ahmed K, Islam Shiblee MN, Zeenat L, Pati F, Ionov L, Chinnakorn A, Nuansing W, Sousa AM, Henriques J, Piedade AP, Blasco E, Li H, Jian B, Ge Q, Demoly F, Qi HJ, André J-C, Nafea M, Fu Y-F, Rolfe B, Tao Y, Wang G, Zolfagharian A. 4D printing roadmap. Smart Mater Struct 2024;33:113501. http://dx.doi.org/10.1088/1361-665X/ad5c22, URL: https://iopscience.iop.org/article/10.1088/1361-665X/ad5c22.

[25] Mousavi S, Howard D, Zhang F, Leng J, Wang CH. Direct 3D printing of highly anisotropic, flexible, constriction-resistive sensors for multidirectional proprioception in soft robots. ACS Appl Mater Interfaces 2020;12:15631–43. http://dx.doi.org/10.1021/acsami.9b21816, URL: https://pubs.acs.org/doi/10.1021/acsami.9b21816.

[26] Rahmatabadi D, Mirasadi K, Bayati A, Khajepour M, Ghasemi I, Baniassadi M, Abrinia K, Bodaghi M, Baghani M. 4D printing thermo-magneto-responsive PETG-Fe3O4 nanocomposites with enhanced shape memory effects. Appl Mater Today 2024;40:102361. http://dx.doi.org/10.1016/j.apmt.2024.102361, URL: https://linkinghub.elsevier.com/retrieve/pii/S2352940724003068.

[27] Zolfaghari A, Purrouhani MR, Zolfagharian A. A response surface methodology study on 4D printing for layered PLA/TPU structures. Prog Addit Manuf 2024. http://dx.doi.org/10.1007/s40964-024-00611-2, URL: https://link.springer.com/10.1007/s40964-024-00611-2.

[28] Rahmatabadi D, Khajepour M, Bayati A, Mirasadi K, Amin Yousefi M, Shegeft A, Ghasemi I, Baniassadi M, Abrinia K, Bodaghi M, Baghani M. Advancing sustainable shape memory polymers through 4D printing of polylactic acid-polybutylene adipate terephthalate blends. Eur Polym J 2024;216:113289. http://dx.doi.org/10.1016/j.eurpolymj.2024.113289, URL: https://linkinghub.elsevier.com/retrieve/pii/S0014305724005500.

[29] El Moumen A, Tarfaoui M, Lafdi K. Additive manufacturing of polymer composites: Processing and modeling approaches. Compos Part B: Eng 2019;171:166–82. http://dx.doi.org/10.1016/j.compositesb.2019.04.029, URL: https://linkinghub.elsevier.com/retrieve/pii/S1359836819302653.

[30] Srivastava R, Fasano M, Mohammad Nejad S, Chávez Thielemann H, Chiavazzo E, Asinari P. 3 modeling carbon-based smart materials. In: Charitidis CA, Koumoulos EP, Dragatogiannis DA, editors. Carbon-based smart materials. De Gruyter; 2020, p. 33–80. http://dx.doi.org/10.1515/9783110479133-003, URL: https://www.degruyter.com/document/doi/10.1515/9783110479133-003/html.

[31] Feng Y, Hao H, Lu H, Chow CL, Lau D. Exploring the development and applications of sustainable natural fiber composites: A review from a nanoscale perspective. Compos Part B: Eng 2024;276:111369. http://dx.doi.org/10.1016/j.compositesb.2024.111369, URL: https://linkinghub.elsevier.com/retrieve/pii/S135983682400180X.

[32] Muhammad A, Srivastava R, Koutroumanis N, Semitekolos D, Chiavazzo E, Pappas P-N, Galiotis C, Asinari P, Charitidis CA, Fasano M. Mesoscopic modeling and experimental validation of thermal and mechanical properties of polypropylene nanocomposites reinforced by graphene-based fillers. Macromolecules 2023;56:9969–82. http://dx.doi.org/10.1021/acs.macromol.3c01529, URL: https://pubs.acs.org/doi/10.1021/acs.macromol.3c01529.

[33] Andreozzi A, Asinari P, Barletta A, Bianco V, Bocanegra JA, Brandão PV, Buonomo B, Cappabianca R, Celli M, Chiavazzo E, De Angelis P, Diani A, Filippeschi S, Iasiello M, Manca O, Nardini S, Nonino C, Rossetto L. Heat transfer and thermal energy storage enhancement by foams and nanoparticles. Energies 2023;16:7421. http://dx.doi.org/10.3390/en16217421, URL: https://www.mdpi.com/1996-1073/16/21/7421.

[34] Tümer EH, Erbil HY. Extrusion-based 3D printing applications of PLA composites: A review. Coatings 2021;11:390. http://dx.doi.org/10.3390/coatings11040390, URL: https://www.mdpi.com/2079-6412/11/4/390.

[35] Joseph TM, Kallingal A, Suresh AM, Mahapatra DK, Hasanin MS, Haponiuk J, Thomas S. 3D printing of polylactic acid: recent advances and opportunities. Int J Adv Manuf Technol 2023;125:1015–35. http://dx.doi.org/10.1007/s00170-022-10795-y, URL: https://link.springer.com/10.1007/s00170-022-10795-y.

[36] Muhammad A, Sáenz Ezquerro C, Srivastava R, Asinari P, Laspalas M, Chiminelli A, Fasano M. Atomistic to mesoscopic modelling of thermophysical properties of graphene-reinforced epoxy nanocomposites. Nanomaterials 2023;13:1960. http://dx.doi.org/10.3390/nano13131960, URL: https://www.mdpi.com/2079-4991/13/13/1960.

[37] Commission E, for Research D-G, Innovation, Baas A. What makes a material function? – let me compute the ways – modeling in h2020 LEIT-nMBP programme materials and nanotechnology projects – sixth version – short version. Publications Office of the European Union; 2017, http://dx.doi.org/10.2777/404734.

[38] Marrink SJ, Risselada HJ, Yefimov S, Tieleman DP, De Vries AH. The MARTINI force field: Coarse grained model for biomolecular simulations. J Phys Chem B 2007;111:7812–24. http://dx.doi.org/10.1021/jp071097f, URL: https://pubs.acs.org/doi/10.1021/jp071097f.

[39] Hossain D, Tschopp M, Ward D, Bouvard J, Wang P, Horstemeyer M. Molecular dynamics simulations of deformation mechanisms of amorphous polyethylene. Polymer 2010;51:6071–83. http://dx.doi.org/10.1016/j.polymer.2010.10.009, URL: https://linkinghub.elsevier.com/retrieve/pii/S0032386110008839.

[40] Humphrey W, Dalke A, Schulten K. VMD: Visual molecular dynamics. J Mol Graph 1996;14:33–8. http://dx.doi.org/10.1016/0263-7855(96)00018-5, URL: https://linkinghub.elsevier.com/retrieve/pii/0263785596000185.

[41] Plimpton S. Fast parallel algorithms for short-range molecular dynamics. J Comput Phys 1995;117:1–19. http://dx.doi.org/10.1006/jcph.1995.1039, URL: https://linkinghub.elsevier.com/retrieve/pii/S002199918571039X.

[42] Nosé S. A unified formulation of the constant temperature molecular dynamics methods. J Chem Phys 1984;81:511–9. http://dx.doi.org/10.1063/1.447334, URL: https://pubs.aip.org/jcp/article/81/1/511/607222/A-unified-formulation-of-the-constant-temperature.

[43] Hoover WG. Canonical dynamics: Equilibrium phase-space distributions. Phys Rev A 1985;31:1695–7. http://dx.doi.org/10.1103/PhysRevA.31.1695, URL: https://link.aps.org/doi/10.1103/PhysRevA.31.1695.

[44] Timoshenko SP, Goodier JN, Abramson HN. Theory of elasticity (3rd ed.). J Appl Mech 1970;37. http://dx.doi.org/10.1115/1.3408648, 888–888. URL: https://asmedigitalcollection.asme.org/appliedmechanics/article/37/3/888/427761/Theory-of-Elasticity-3rd-ed.

[45] Müller-Plathe F. A simple nonequilibrium molecular dynamics method for calculating the thermal conductivity. J Chem Phys 1997;106:6082–5. http://dx.doi.org/10.1063/1.473271, URL: https://pubs.aip.org/jcp/article/106/14/6082/181799/A-simple-nonequilibrium-molecular-dynamics-method.

[46] Mohammad Nejad S, Srivastava R, Bellussi FM, Chávez Thielemann H, Asinari P, Fasano M. Nanoscale thermal properties of carbon nanotubes/epoxy composites by atomistic simulations. Int J Therm Sci 2021;159:106588. http://dx.doi.org/10.1016/j.ijthermalsci.2020.106588, URL: https://linkinghub.elsevier.com/retrieve/pii/S1290072920310383.

[47] Zhou L-P, Wang B-X, Peng X-F, Du X-Z, Yang Y-P. On the specific heat capacity of CuO nanofluid. Adv Mech Eng 2010;2:172085. http://dx.doi.org/10.1155/2010/172085, URL: http://journals.sagepub.com/doi/10.1155/2010/172085.

[48] Zábranský M, Růžička V, Domalski ES. Heat capacity of liquids: Critical review and recommended values. Supplement I. J Phys Chem Ref Data 2001;30:1199–689. http://dx.doi.org/10.1063/1.1407866, URL: https://pubs.aip.org/jpr/article/30/5/1199/241843/Heat-Capacity-of-Liquids-Critical-Review-and.

[49] Paulechka YU. Heat capacity of room-temperature ionic liquids: A critical review. J Phys Chem Ref Data 2010;39:033108. http://dx.doi.org/10.1063/1.3463478, URL: https://pubs.aip.org/jpr/article/39/3/033108/377835/Heat-Capacity-of-Room-Temperature-Ionic-Liquids-A.

[50] Mori T, Tanaka K. Average stress in matrix and average elastic energy of materials with misfitting inclusions. Acta Metall 1973;21:571–4. http://dx.doi.org/10.1016/0001-6160(73)90064-3, URL: https://linkinghub.elsevier.com/retrieve/pii/0001616073900643.

[51] PRIMAVALUE. Primavalue™ PLA. 2024, URL: https://primacreator.com/products/primavalue%E2%84%A2-pla?variant=61780172555. (Accessed 27 July 2024).

[52] ASTM. Standard test method for tensile properties of thin plastic sheeting. Standard, West Conshohocken, USA: American Society for Testing and Materials; 2010, http://dx.doi.org/10.1520/D0882-02.

[53] ISO. Plastics – determination of thermal conductivity and thermal diffusivity – transient plane heat source (hot disc) method. Standard, Geneva, CH: International Organization for Standardization; 2009, URL: https://www.iso.org/standard/81836.html.

[54] Rasband WS. Imagej. 2024, URL: https://imagej.net/ij/.

[55] Schneider CA, Rasband WS, Eliceiri KW. NIH Image to ImageJ: 25 years of image analysis. Nature Methods 2012;9:671–5. http://dx.doi.org/10.1038/nmeth.2089, URL: https://www.nature.com/articles/nmeth.2089.

[56] Chen GL, Yanamandra K, Gupta N. Artificial neural networks framework for detection of defects in 3D-printed fiber reinforcement composites. JOM 2021;73:2075–84. http://dx.doi.org/10.1007/s11837-021-04708-9, URL: https://link.springer.com/10.1007/s11837-021-04708-9.

[57] Zienkiewicz OC, Taylor RL, Zhu JZ. The finite element method: its basis and fundamentals. Elsevier; 2013, http://dx.doi.org/10.1016/C2009-0-24909-9, URL: https://linkinghub.elsevier.com/retrieve/pii/C20090249099.

[58] Micromechanics Plugin for Abaqus/CAE. 2017, URL: https://www.3ds.com/products/simulia.

[59] Yvonnet J. Computational homogenization of heterogeneous materials with finite elements. Solid mechanics and its applications, vol. 258, Cham: Springer International Publishing; 2019, http://dx.doi.org/10.1007/978-3-030-18383-7, URL: http://link.springer.com/10.1007/978-3-030-18383-7.

[60] Systémes D. Simulia. 2023, URL: https://www.3ds.com/products/simulia.

[61] Garzon-Hernandez S, Arias A, Garcia-Gonzalez D. A continuum constitutive model for FDM 3D printed thermoplastics. Compos Part B: Eng 2020;201:108373. http://dx.doi.org/10.1016/j.compositesb.2020.108373, URL: https://linkinghub.elsevier.com/retrieve/pii/S1359836820334193.

[62] Safavi HR, Amiri A, Baniassadi M, Zolfagharian A, Baghani M. An anisotropic constitutive model for fiber reinforced salt-sensitive hydrogels. Mech Adv Mater Struct 2023;30:4814–27. http://dx.doi.org/10.1080/15376494.2022.2106523, URL: https://www.t{andf}online.com/doi/full/10.1080/15376494.2022.2106523.

[63] Li X, Xiao T, Xiao N. The application of nonlocal theory method in the coarse-grained molecular dynamics simulations of long-chain polylactic acid. Acta Mech Solida Sin 2017;30:630–7. http://dx.doi.org/10.1016/j.camss.2017.10.003, URL: http://linkinghub.elsevier.com/retrieve/pii/S0894916617301064.

[64] Xiang H, Wang Y, Yang W, Hu C, Mu Y, Li J. Study of the mechanical and thermal properties of poly(lactic acid) and poly(ethylene glycol) block copolymer with molecular dynamics. Int J Polym Anal Charact 2010;15:235–44. http://dx.doi.org/10.1080/10236661003746405, URL: http://www.t{andf}online.com/doi/abs/10.1080/10236661003746405.

[65] Xie R, Weisen AR, Lee Y, Aplan MA, Fenton AM, Masucci AE, Kempe F, Sommer M, Pester CW, Colby RH, Gomez ED. Glass transition temperature from the chemical structure of conjugated polymers. Nat Commun 2020;11:893. http://dx.doi.org/10.1038/s41467-020-14656-8, URL: https://www.nature.com/articles/s41467-020-14656-8.

[66] Farah S, Anderson DG, Langer R. Physical and mechanical properties of PLA, and their functions in widespread applications — A comprehensive review. Adv Drug Deliv Rev 2016;107:367–92. http://dx.doi.org/10.1016/j.addr.2016.06.012, URL: https://linkinghub.elsevier.com/retrieve/pii/S0169409X16302058.

[67] Mortazavi B, Hassouna F, Laachachi A, Rajabpour A, Ahzi S, Chapron D, Toniazzo V, Ruch D. Experimental and multiscale modeling of thermal conductivity and elastic properties of PLA/expanded graphite polymer nanocomposites. Thermochim Acta 2013;552:106–13. http://dx.doi.org/10.1016/j.tca.2012.11.017, URL: https://linkinghub.elsevier.com/retrieve/pii/S0040603112005412.

[68] Laureto J, Tomasi J, King JA, Pearce JM. Thermal properties of 3-D printed polylactic acid-metal composites. Prog Addit Manuf 2017;2:57–71. http://dx.doi.org/10.1007/s40964-017-0019-x, URL: http://link.springer.com/10.1007/s40964-017-0019-x.

[69] Guo R, Ren Z, Bi H, Xu M, Cai L. Electrical and thermal conductivity of polylactic acid (PLA)-based biocomposites by incorporation of nano-graphite fabricated with fused deposition modeling. Polymers 2019;11:549. http://dx.doi.org/10.3390/polym11030549, URL: https://www.mdpi.com/2073-4360/11/3/549.

[70] Zmeskal O, Marackova L, Lapcikova T, Mencik P, Prikryl R. Thermal properties of samples prepared from polylactic acid by 3D printing. Smolenice, Slovakia; 2020, 020022. http://dx.doi.org/10.1063/5.0033857, URL: https://pubs.aip.org/aip/acp/article/740039.

[71] Ruiz L, Xia W, Meng Z, Keten S. A coarse-grained model for the mechanical behavior of multi-layer graphene. Carbon 2015;82:103–15. http://dx.doi.org/10.1016/j.carbon.2014.10.040, URL: https://linkinghub.elsevier.com/retrieve/pii/S0008622314010021.

[72] Shang J-J, Yang Q-S, Liu X. New coarse-grained model and its implementation in simulations of graphene assemblies. J Chem Theory Comput 2017;13:3706–14. http://dx.doi.org/10.1021/acs.jctc.7b00051, URL: https://pubs.acs.org/doi/10.1021/acs.jctc.7b00051.

[73] Li Q-Y, Xia K, Zhang J, Zhang Y, Li Q, Takahashi K, Zhang X. Measurement of specific heat and thermal conductivity of supported and suspended graphene by a comprehensive Raman optothermal method. Nanoscale 2017;9:10784–93. http://dx.doi.org/10.1039/C7NR01695F, URL: http://xlink.rsc.org/?DOI=C7NR01695F.

[74] Zhan N, Chen B, Li C, Shen PK. Molecular dynamics simulations of the thermal conductivity of graphene for application in wearable devices. Nanotechnology 2019;30:025705. http://dx.doi.org/10.1088/1361-6528/aae98b, URL: https://iopscience.iop.org/article/10.1088/1361-6528/aae98b.

[75] Suter JL, Sinclair RC, Coveney PV. Principles governing control of aggregation and dispersion of graphene and graphene oxide in polymer melts. Adv Mater 2020;32:2003213. http://dx.doi.org/10.1002/adma.202003213, URL: https://onlinelibrary.wiley.com/doi/10.1002/adma.202003213.

[76] Smith AT, LaChance AM, Zeng S, Liu B, Sun L. Synthesis, properties, and applications of graphene oxide/reduced graphene oxide and their nanocomposites. Nano Mater Sci 2019;1:31–47. http://dx.doi.org/10.1016/j.nanoms.2019.02.004, URL: https://linkinghub.elsevier.com/retrieve/pii/S2589965119300042.

[77] Meng Z, Soler-Crespo RA, Xia W, Gao W, Ruiz L, Espinosa HD, Keten S. A coarse-grained model for the mechanical behavior of graphene oxide. Carbon 2017;117:476–87. http://dx.doi.org/10.1016/j.carbon.2017.02.061, URL: https://linkinghub.elsevier.com/retrieve/pii/S0008622317301902.

[78] Ji XL, Jing JK, Jiang W, Jiang BZ. Tensile modulus of polymer nanocomposites. Polym Eng Sci 2002;42:983–93. http://dx.doi.org/10.1002/pen.11007, URL: https://4spepublications.onlinelibrary.wiley.com/doi/10.1002/pen.11007.

[79] Zamanian M, Ashenai Ghasemi F, Mortezaei M. Interphase characterization and modeling of tensile modulus in epoxy/silica nanocomposites. J Appl Polym Sci 2021;138:49755. http://dx.doi.org/10.1002/app.49755, URL: https://onlinelibrary.wiley.com/doi/10.1002/app.49755.

[80] Zare Y, Garmabi H. A developed model to assume the interphase properties in a ternary polymer nanocomposite reinforced with two nanofillers. Compos Part B: Eng 2015;75:29–35. http://dx.doi.org/10.1016/j.compositesb.2015.01.031, URL: https://linkinghub.elsevier.com/retrieve/pii/S1359836815000487.

[81] Zare Y. Modeling approach for tensile strength of interphase layers in polymer nanocomposites. J Colloid Interface Sci 2016;471:89–93. http://dx.doi.org/10.1016/j.jcis.2016.03.029, URL: https://linkinghub.elsevier.com/retrieve/pii/S0021979716301710.

[82] Boutaleb S, Zaïri F, Mesbah A, Naït-Abdelaziz M, Gloaguen J, Boukharouba T, Lefebvre J. Micromechanics-based modelling of stiffness and yield stress for silica/polymer nanocomposites. Int J Solids Struct 2009;46:1716–26. http://dx.doi.org/10.1016/j.ijsolstr.2008.12.011, URL: https://linkinghub.elsevier.com/retrieve/pii/S0020768308005106.

[83] Shahil KMF, Balandin AA. Graphene–multilayer graphene nanocomposites as highly efficient thermal interface materials. Nano Lett 2012;12:861–7. http://dx.doi.org/10.1021/nl203906r, URL: https://pubs.acs.org/doi/10.1021/nl203906r.

[84] Alexandre M, Dubois P. Polymer-layered silicate nanocomposites: preparation, properties and uses of a new class of materials. Mater Sci Eng: R: Rep 2000;28:1–63. http://dx.doi.org/10.1016/S0927-796X(00)00012-7, URL: https://linkinghub.elsevier.com/retrieve/pii/S0927796X00000127.

[85] Fu S-Y, Feng X-Q, Lauke B, Mai Y-W. Effects of particle size, particle/matrix interface Adhesion and particle loading on mechanical properties of particulate–polymer composites. Compos Part B: Eng 2008;39:933–61. http://dx.doi.org/10.1016/j.compositesb.2008.01.002, URL: https://linkinghub.elsevier.com/retrieve/pii/S135983680800005X.

[86] Young RJ, Kinloch IA, Gong L, Novoselov KS. The mechanics of graphene nanocomposites: A review. Compos Sci Technol 2012;72:1459–76. http://dx.doi.org/10.1016/j.compscitech.2012.05.005, URL: https://linkinghub.elsevier.com/retrieve/pii/S0266353812001789.

[87] Kalaitzidou K, Fukushima H, Miyagawa H, Drzal LT. Flexural and tensile moduli of polypropylene nanocomposites and comparison of experimental data to Halpin–Tsai and Tandon–Weng models. Polym Eng Sci 2007;47:1796–803. http://dx.doi.org/10.1002/pen.20879, URL: https://4spepublications.onlinelibrary.wiley.com/doi/10.1002/pen.20879.

[88] Jun Y-S, Um JG, Jiang G, Lui G, Yu A. Ultra-large sized graphene nano-platelets (GnPs) incorporated polypropylene (PP)/GnPs composites engineered by melt compounding and its thermal, mechanical, and electrical properties. Compos Part B: Eng 2018;133:218–25. http://dx.doi.org/10.1016/j.compositesb.2017.09.028, URL: https://linkinghub.elsevier.com/retrieve/pii/S1359836816321758.

[89] Innes JR, Young RJ, Papageorgiou DG. Graphene nanoplatelets as a replacement for carbon black in rubber compounds. Polymers 2022;14:1204. http://dx.doi.org/10.3390/polym14061204, URL: https://www.mdpi.com/2073-4360/14/6/1204.

[90] Prajapati H, Ravoori D, Woods RL, Jain A. Measurement of anisotropic thermal conductivity and inter-layer thermal contact resistance in polymer fused deposition modeling (FDM). Addit Manuf 2018;21:84–90. http://dx.doi.org/10.1016/j.addma.2018.02.019, URL: https://linkinghub.elsevier.com/retrieve/pii/S2214860417305456.

[91] Elkholy A, Rouby M, Kempers R. Characterization of the anisotropic thermal conductivity of additively manufactured components by fused filament fabrication. Prog Addit Manuf 2019;4:497–515. http://dx.doi.org/10.1007/s40964-019-00098-2, URL: http://link.springer.com/10.1007/s40964-019-00098-2.

[92] Song Y, Li Y, Song W, Yee K, Lee K-Y, Tagarielli V. Measurements of the mechanical response of unidirectional 3D-printed PLA. Mater Des 2017;123:154–64. http://dx.doi.org/10.1016/j.matdes.2017.03.051, URL: https://linkinghub.elsevier.com/retrieve/pii/S0264127517302976.

[93] Cataldi P, Bayer IS, Nanni G, Athanassiou A, Bonaccorso F, Pellegrini V, Del Rio Castillo AE, Ricciardella F, Artyukhin S, Tronche M-A, Gogotsi Y, Cingolani R. Effect of graphene nano-platelet morphology on the elastic modulus of soft and hard biopolymers. Carbon 2016;109:331–9. http://dx.doi.org/10.1016/j.carbon.2016.08.026, URL: https://linkinghub.elsevier.com/retrieve/pii/S0008622316306819.

[94] Silva M, Pinho IS, Covas JA, Alves NM, Paiva MC. 3D printing of graphene-based polymeric nanocomposites for biomedical applications. Funct Compos Mater 2021;2:8. http://dx.doi.org/10.1186/s42252-021-00020-6, URL: https://functionalcompositematerials.springeropen.com/articles/10.1186/s42252-021-00020-6.

[95] Chiminelli A, Radović I, Fasano M, Fantoni A, Laspalas M, Kalinić A, Provenzano M, Fernandes M. Modeling carbon-based nanomaterials (cnms) and derived composites and devices. Sensors 2024;24:7665.

[96] Thompson AP, Aktulga HM, Berger R, Bolintineanu DS, Brown WM, Crozier PS, in 't Veld PJ, Kohlmeyer A, Moore SG, Nguyen TD, Shan R, Stevens MJ, Tranchida J, Trott C, Plimpton SJ. LAMMPS - a flexible simulation tool for particle-based materials modeling at the atomic, meso, and continuum scales. Comp Phys Comm 2022;271:10817.